Mechanical Systems and Signal Processing 262 (2027) 115145

Contents lists available at ScienceDirect

Mechanical Systems and Signal Processing

journal homepage: www.elsevier.com/locate/ymssp

Full Length Article

Estimating diffusive body-wave properties in bounded concrete members using an energy-contribution-based image-source method

Hao Cheng [a,*], Katrin Löer [b], Max A.N. Hendriks [a,c], Yuguang Yang [a]

[a] Department of Engineering Structures, Faculty of Civil Engineering and Geosciences, Delft University of Technology, 2628 CN Delft, the Netherlands
[b] Department of Geoscience and Engineering, Faculty of Civil Engineering and Geosciences, Delft University of Technology, 2628 CN Delft, the Netherlands
[c] Department of Structural Engineering, Faculty of Engineering, Norwegian University of Science and Technology, 7491 Trondheim, Norway

ARTICLE INFO

Communicated by Filippo Ubertini

Keywords:
Body waves
Boundary reflections
Concrete
Diffusivity
Dissipation

ABSTRACT

Reliable characterization of diffusive body-wave properties in concrete is essential for damage assessment and diffuse-wave-based imaging. However, existing approaches either neglect boundary reflections, thereby biasing the fitted properties, or rely on full analytical solutions for bounded domains, which greatly increase the complexity of curve fitting. In this study, an energy-contribution-based image-source method is proposed for concrete members with external planar concrete-air boundaries. The method retains only the image sources whose energy contributions are sufficiently large, thereby reducing model complexity while maintaining agreement with the bounded-domain solution. The method is evaluated using four concrete members with multiple pairs of ultrasonic sensors embedded. The experimental comparisons show that neglecting reflected energy underestimates both diffusivity and dissipation, with the strongest influence occurring at low frequencies. The comparisons across the four members show that retaining the dominant reflection terms achieves close agreement with the cuboid-domain benchmark, with only marginal improvement from additional reflections. These comparisons, together with the estimated reflection contributions, suggest approximately 30% as an empirical reference level for reflection screening in similar configurations. For the retained reflection configurations, the mean relative differences of diffusivity and dissipation remain below 2% for all four members when compared with the cuboid-medium reference solution, while the computational cost is much lower than that of the full analytical formulation. Across all members, diffusivity decreases with increasing frequency, and dissipation increases with increasing frequency. These results indicate that the proposed method provides a benchmark-consistent and computationally efficient approach to estimate frequency-dependent diffusive properties in bounded concrete members with approximately planar free concrete-air boundaries in the monitored region.

1. Introduction

Concrete is widely used as the dominant construction material worldwide. Over the past two decades, there has been growing

* Corresponding author.
E-mail address: haojaysonshing@gmail.com (H. Cheng).

https://doi.org/10.1016/j.ymssp.2026.115145
Received 2 April 2026; Received in revised form 2 October 2026; Accepted 28 October 2026
Available online 7 November 2026
0888-3270/© 2026 The Author(s). Published by Elsevier Ltd. This is an open access article under the CC BY license (http://creativecommons.org/licenses/by/4.0/).

interest in the non-destructive and real-time monitoring of the structural integrity of concrete structures, especially concrete infrastructures [1–3]. Among the available techniques, ultrasonic methods have emerged as one of the most promising approaches because of their sensitivity to minor structural defects [4]. Ultrasonic methods can be broadly divided into those based on ballistic waves [5] and those based on diffuse waves [6]. Ballistic-wave-based methods require a wavelength comparable to the size of the damage to achieve high sensitivity [5], which usually implies the use of frequencies in the range of several hundred kilohertz for early crack detection. However, high-frequency body waves undergo significant attenuation in concrete, which has led to increasing interest in the use of diffuse waves for concrete monitoring [7–9]. Diffuse waves, which arise from multiple scattering events, dominate the coda portion of a recorded signal [10]. Because they have undergone extensive scattering by heterogeneities in concrete, they travel much longer paths than ballistic waves and are therefore highly sensitive to weak perturbations in the medium, such as stress changes [11,12] and temperature changes [13–15], owing to the cumulative effect of these perturbations on travel-time variations along the wave path.

Applications of diffuse waves in concrete monitoring can be broadly divided into two categories: global monitoring of a region by exploiting its diffusive properties [16,17], and disturbance localization using coda wave interferometry (CWI) in conjunction with sensitivity kernels [18,19]. In this context, the diffusive properties refer to diffusivity and dissipation, which characterize the rate of energy transport and the amount of energy loss during transport, respectively. The former line of research aims to characterize changes in the *meso*-structure of the material through variations in these properties. The latter uses elastic waves within selected time windows and sensitivity kernels to localize disturbances within a sensor network. Since the sensitivity kernels used in such studies are generally constructed on the basis of diffusive properties [20], both categories rely on the accurate estimation of these properties.

In previous studies, the diffusive properties of heterogeneous cementitious materials have been extracted by fitting the evolution of wave energy with one-, two-, or three-dimensional diffusion equations, depending on the specimen geometry and the measurement configuration. As summarized in Table 1, these studies have been carried out mainly on conventional concrete and cement paste. However, most of them treated the medium as effectively unbounded and therefore did not explicitly account for boundary reflections. Examples include the concrete cylinders and prisms studied in [21–26], as well as more recent concrete beams, prisms, and cylinders analysed using unbounded diffusion formulations [16,27–32]. Although analytical solutions incorporating Neumann boundary conditions have been developed for two-dimensional rectangular domains and three-dimensional cuboid domains, these formulations require all reflected energy to be taken into account, which greatly increases the complexity of the fitting procedure. This difficulty has also been noted in previous work; for example, Deroo et al. [33] reported that the larger variations obtained with the finite-domain solution were probably related to the higher model complexity and the more complicated nonlinear fitting procedure. The availability

Table 1
Summary of previous studies on the extraction of diffusive properties in cementitious materials using diffusion equations.

Reference	Specimen [mm]	Dimensionality of the diffusion equation	Boundary reflections considered in the diffusion equation?
Anugonda et al. 2001 [34]	Concrete cylinder Ø50 × 460	1	No
Becker et al. 2003 [35]	Cement paste cylinder with glass beads Ø76× (from 14 to 16)	2	No
Ramamoorthy et al. 2004 [36]	Concrete slab 609.6 × 609.6 × 203.2	2	Yes, full analytical solution in a 2D rectangular domain
Schubert and Koehler 2004 [21]	Concrete cylinder Ø50 × 460	1	No
Deroo et al. 2010 [33]	Concrete prism 75 × 75 × 46	3	Yes, full analytical solution in a 3D cuboid domain
Quiviger et al. 2012 [22]	Concrete prism 150 × 150 × 600	2	No
In et al. 2013 [37]	Concrete prism 127 × 127 × 457	2	Yes, full analytical solution in a 2D rectangular domain
Payan et al. 2013 [23]	Concrete prism 150 × 150 × 600	2	No
Quiviger et al. 2013 [24]	Concrete prism 150 × 150 × 600	2	No
Seher et al. 2013 [38]	Concrete prism 254 × 330 × 609.6	2	Yes, full analytical solution in a 2D rectangular domain
Shokouhi and Lorenz 2014 [25]	Concrete prism 200 × 200 × 600	1	No
Hilloulin et al. 2016 [39]	Mortar prism 70 × 70 × 280	3	Yes, full analytical solution in a 3D cuboid domain
Yim et al. 2016 [26]	Cement paste Ø100 × 40	1	No
In et al. 2017 [40]	Concrete beam 152 × 254 × 2438	2	Yes, full analytical solution in a 2D rectangular domain
Ahn et al. 2019 [27]	Concrete prism 300 × 300 × 600	3	No
Jiang et al. 2019 [28]	Concrete beam 300 × 870 × 5960	3	No
Tinoco and Pinto 2021 [29]	Concrete beam 150 × 220 × 1700	3	No
Ahn et al. 2022 [16]	Concrete prism 300 × 300 × 600	3	No
Basu and Sasmal 2024 [30]	Concrete prism 150 × 150 × 200	2	No
Ahn et al. 2025 [31]	Concrete cylinder Ø100 × 200	3	No
Yang et al. 2025 [32]	Concrete cylinder Ø150 × 300	3	No

of these full bounded-domain solutions demonstrates that the theoretical representation of boundary reflections is well established; however, theoretical completeness does not by itself determine whether the full formulation is practically necessary for a particular concrete-monitoring configuration. In particular, the complete theory does not provide an operational criterion for identifying which reflected-energy terms materially affect the inferred diffusivity and dissipation and which can be omitted without considerably changing the fitted results. This decision depends on the sensor-boundary geometry, diffusivity, and lapse time, while diffusivity is itself one of the parameters to be estimated. Therefore, the unresolved problem is not the absence of diffusion theory or the absence of image-source representations. Rather, it is the lack of a practical fitting strategy that can account for the dominant boundary-reflection effects without introducing the full complexity of bounded-domain analytical solutions. This gap is particularly relevant for diffuse-wave-based characterization of cementitious materials, where diffusivity and dissipation often need to be fitted repeatedly over multiple sensor pairs and frequency bands.

Accordingly, this study develops an energy-contribution-guided image-source model-reduction strategy for estimating the diffusive properties of body waves in bounded concrete members. The study does not modify the governing diffusion equation or introduce a new boundary-condition or image-source theory; instead, it addresses how the established image-source representation can be implemented more practically in repeated parameter estimation. The method treats reflected energy as originating from image sources [20,41–43], but, unlike full analytical solutions for bounded domains, it retains only those image sources that make non-negligible energy contributions. For each monitoring configuration, candidate image sources are constructed from the known boundary geometry, and their expected contributions relative to the direct energy are assessed before nonlinear fitting using the sensor configuration, expected diffusivity range, and fitting-time interval. Because the retained image-source locations and propagation distances are determined by the specimen geometry, the reduction does not introduce additional parameters to be estimated from the measured waveform. In this way, boundary reflections can be incorporated without requiring all possible reflected paths to be included, thereby enabling a simplified yet accurate fitting model with lower mathematical complexity. To make this selection systematic, an energy-contribution criterion is introduced to screen the candidate image sources and determine which reflections should be retained in the fitting process. Compared with previous diffusion-based studies, the main strength of the present method lies in its ability to account for boundary reflections in a computationally efficient manner without relying on the full analytical solution for a bounded domain. The evaluation focuses on the agreement of the estimated diffusivity and dissipation with the full cuboid-domain diffusion solution and on the computational cost of parameter fitting. The performance of these estimates in downstream damage-detection or localization tasks is not assessed in this study. Beam I is first used to establish and demonstrate the contribution-based screening procedure, with the full cuboid-domain solution serving as the benchmark for quantifying model-reduction error rather than as an independent physical ground truth; the same procedure is subsequently assessed in three additional members from the tested structural system. The contribution of the study therefore lies in translating a theoretically complete boundary treatment into a practical fitting strategy and in quantifying its benchmark agreement and computational benefit under structural-scale concrete-monitoring conditions, rather than in proposing a new diffusion theory or a universally applicable numerical screening threshold.

2. Theoretical background

In a heterogeneous material such as concrete, the wave transport regime is strongly influenced by the wavelength λ and the average size of heterogeneities —d. In concrete, the characteristic size of heterogeneities is typically associated with the size of aggregates and air voids. Depending on the relation between λ and —d, scattered elastic waves in concrete are generally classified into three regimes [44,45]:

- $\lambda \gg \overline{d}$: when the wavelength is much greater than the average diameter of heterogeneities, the propagating wave encounters limited interactions with the heterogeneities. This regime is known as the Rayleigh regime, or low-frequency limit. The Born approximation [45], or its analogue, Rayleigh-Gans approximation [46,47], is generally applicable in this regime.
- $\lambda \cong \overline{d}$: when the wavelength is of a size that is comparable to the average diameter of heterogeneities, the wave has sufficient interaction with the heterogeneities. This regime is often referred to as the stochastic regime. The Born approximation may still provide an approximate description under such conditions [45].
- $\lambda \ll \overline{d}$: when the wavelength is much smaller than the average diameter of heterogeneities, the wave strongly interacts with the heterogeneities. This regime is known as the geometrical regime, or high-frequency limit. In this regime, the Born approximation generally fails [47,48], and Anderson localization [49,50] might be observed.

For scattering media, energy transport can be described using the radiative transfer equation (RTE) [51]. However, the complexity of the RTE limits its practical use in engineering applications. As a simpler alternative, the diffusion equation [52] is commonly adopted when the wave field has entered the diffusive regime within a multiple-scattering medium [53–55]. This scalar equation has been widely used to describe the transport of various forms of energy, including electromagnetic waves [56], acoustic waves [57], and elastic waves [58].

2.1. Diffusion equation in infinite and cuboid media

The governing equation for diffusion can be written in the following form [41,59]:

$$\frac{\partial E(\mathbf{x},t)}{\partial t} = D\nabla^2 E(\mathbf{x},t) - \sigma E(\mathbf{x},t) + E_0\delta(\mathbf{x}-\mathbf{x}_0)\delta(t) \quad , \tag{1}$$

where t represents time and $\mathbf{x}$ is the spatial vector. $E(\mathbf{x},t)$ is the transport energy at location $\mathbf{x}$ and time t, and E_0 represents the deposited impulse energy at the initial location at time $t = 0$ [41]. The parameters D and σ represent the diffusivity and dissipation, respectively, which characterize the energy transport process. The diffusivity quantifies how quickly energy spreads through the medium [6]. In this context, the diffusivity can be viewed as a measure similar to the "spreading velocity" of the diffusion halo [17]. In the absence of dissipation, the pure diffusion process generally obeys energy conservation [34]. In concrete, dissipation is likely caused by a combination of viscous dissipation and internal friction [60]. Unlike pure diffusion, the dissipation process does not conserve energy.

In an infinite three-dimensional medium, the solution of Eq. (1) is given by [41]:

$$E(r,t) = \frac{E_0}{(4\pi Dt)^{\frac{3}{2}}} e^{\frac{-r^2}{4Dt} - \sigma t} \quad , \tag{2}$$

where r represents the distance between the source and receiver. For a three-dimensional cuboid medium, the solution of Eq. (1) is given as [33,36,39]:

$$\begin{aligned} E(\mathbf{a}_S,\mathbf{a}_R,t) = E_0' e^{-\sigma t} \times & \left[1 + 2\sum_{n=1}^{\infty} \cos\left(\frac{n\pi x_S}{L}\right)\cos\left(\frac{n\pi x_R}{L}\right) e^{-D\left(\frac{n\pi}{L}\right)^2 t}\right] \\ \times & \left[1 + 2\sum_{n=1}^{\infty} \cos\left(\frac{n\pi y_S}{H}\right)\cos\left(\frac{n\pi y_R}{H}\right) e^{-D\left(\frac{n\pi}{H}\right)^2 t}\right] \\ \times & \left[1 + 2\sum_{n=1}^{\infty} \cos\left(\frac{n\pi z_S}{W}\right)\cos\left(\frac{n\pi z_R}{W}\right) e^{-D\left(\frac{n\pi}{W}\right)^2 t}\right] \quad , \end{aligned} \tag{3}$$

where E_0' denotes the volume-averaged energy density immediately after the source impulse, obtained by dividing the total deposited energy E_0 by the volume of the cuboid, $\mathbf{a}_S$ and $\mathbf{a}_R$ denote the position vectors of the source and receiver, with coordinates (x_S,y_S,z_S) and (x_R,y_R,z_R), respectively. The parameters L, H, and W represent the length, height, and width of the concrete specimen. The logarithmic form of Eq. (2) and Eq. (3) is commonly employed to fit the diffusive properties.

2.2. Diffusion equation in a concrete member with multiple external planar boundaries

In the presence of complex boundary conditions, solving the diffusion equation exactly requires accounting for the geometry of the domain [61]. In this study, the term "external planar boundaries" refers to the external concrete-air boundaries of the member, such as the top, bottom, side, front, and back surfaces, rather than to internal heterogeneities, air voids, or solid–solid interfaces inside the concrete. When these external boundaries are approximately planar, the diffusion field can be approximated by superimposing the energy from the real source and the reflected energy represented by image sources [20,41,42], as illustrated in Fig. 1. It should be noted that the image source method is applicable only to geometries formed by planar boundaries [62]. Because the acoustic impedance of concrete is much higher than that of air, the transmission of elastic-wave energy from concrete into air is expected to be very small. In the present study, the acoustic impedance ratio between concrete and air is taken to be on the order of 10^4 [16], so that the transmitted energy is negligible compared with the reflected energy. Therefore, the external concrete-air boundaries of the tested members are approximated as fully reflecting boundaries. This assumption is intended for monitored regions where the dominant nearby boundaries are exposed concrete-air interfaces. It should not be applied without modification to soil-contact or partially absorbing boundaries. If the boundaries are partially reflecting or absorbing, the reflected energy would be reduced and the present formulation would need to be modified accordingly, for example by introducing a characteristic coefficient depending on the nature of the boundary condition [20]. The present study is restricted to the fully reflecting approximation; extensions to partially reflecting or absorbing boundaries are left for future investigation.

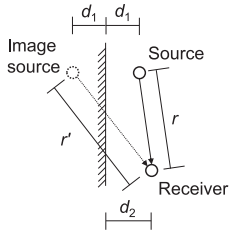


Fig. 1. Schematic representation of energy superposition in the medium with a planar boundary.

The transport energy contributed by the real source and its image source can be expressed in the following form [20]:

$$E_{\text{total}}(r, r', t) = E(r, t) + E(r', t) \quad . \tag{4}$$

where r' represents the distance between the image source and receiver. After substituting Eq. (2) into Eq. (4), the diffusion equation for a medium with one planar boundary can be approximated as follows:

$$E_{\text{total}}(r, r', t) = \frac{E_0}{(4\pi Dt)^{\frac{3}{2}}} e^{\frac{-r^2}{4Dt} - \sigma t} \left(1 + e^{\frac{-\left[(r')^2 - r^2\right]}{4Dt}}\right) \quad . \tag{5}$$

As shown in Eq. (5), the contribution of an image source to the energy produced by the real source is calculated as $\exp\{-[(r')^2-r^2]/(4Dt)\}$ multiplied by the energy produced by the real source. In the case with multiple planar boundaries, the expression becomes:

$$E_{\text{total}}\left(r, r'_j, t\right) = \frac{E_0}{(4\pi Dt)^{\frac{3}{2}}} e^{\frac{-r^2}{4Dt} - \sigma t} \left(1 + \sum_{j=1}^{N} e^{\frac{-\left[\left(r'_j\right)^2 - r^2\right]}{4Dt}}\right) \quad , \tag{6}$$

where N represents the number of image sources. The determination of N will be explained in Section 4.1.

3. Experimental setup and signal processing

3.1. Concrete members, sensor layouts, and data acquisition

In this paper, four geopolymer concrete members are used to assess the proposed method. Two of them are individual prefabricated beams, while the other two are beams within a slab. These members are made of an environmentally friendly cementitious material, namely alkali-activated (geopolymer) concrete [63]. Each member consists of two components: a prestressed beam with a height of 300 mm and a cast-in-situ topping layer. The prestressed beam is manufactured in a prefabricated concrete plant. The cast-in-situ layer is applied 28 days after casting of the prestressed beam. The geopolymer concrete used in the topping layer was supplied by a commercial company and had a different composition from that used for the prestressed beam.

The piezoelectric sensors, whose resonant frequency is around 80 kHz [64], are embedded in these members to serve as transmitters and receivers. Each sensor comprises a PZT patch, a waterproof copper package, and two protective marble blocks. In all members, the sensors are situated at a minimum distance of 77 mm from the external concrete-air boundaries. This distance is mainly

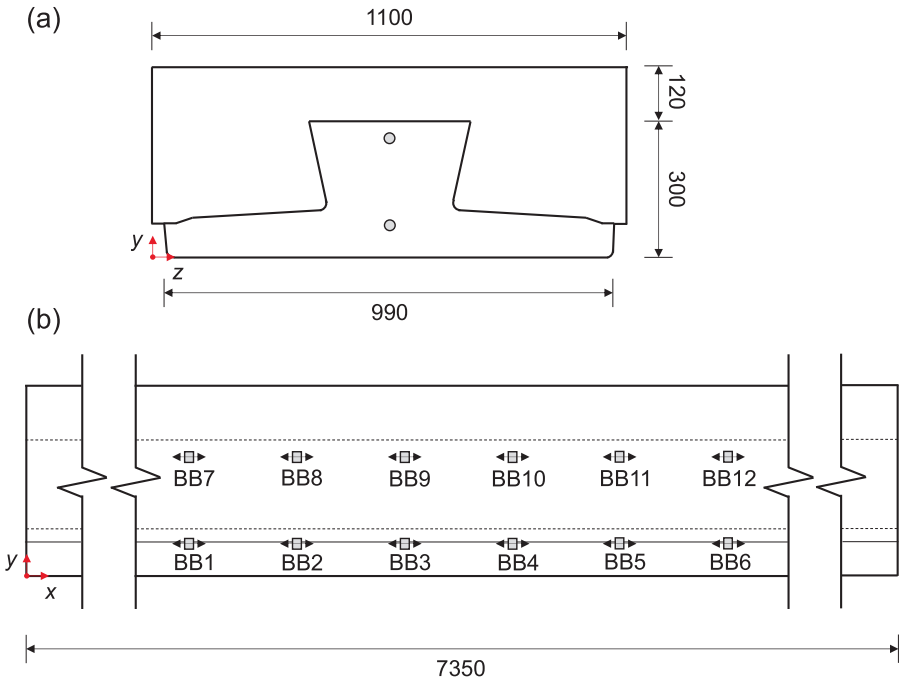


Fig. 2. Dimensions of Beam I and sensor layout (unit: mm; the black arrow on each sensor indicates its polarization direction). (a) Cross-sectional view. (b) Front view.

determined by the practical installation condition: the sensors were fixed to the lower part of the reinforcement cage, and the corresponding concrete cover thickness was 77 mm. In addition to this construction-related reason, this distance also helps reduce the influence of surface waves on the measured signals. Given that the frequency of interest is higher than 50 kHz and the Rayleigh wave velocity in concrete is approximately 2300 m/s [65], the maximum effective depth of penetration for Rayleigh waves is approximately 46 mm [66]. This depth is smaller than 77 mm, indicating that the contribution of Rayleigh wave-related energy transport to the present measurements can be neglected. During the data acquisition, the input electrical signal for sensor activation is a one-cycle square pulse with a duration of 18.5 μs and an amplitude of 200 V. The sampling rate is 3 MHz, and the maximum duration of the recorded signal is 3000 μs (9000 samples). Random noise is reduced using a stacking process, in which five repeated signals are averaged.

In the first beam, denoted Beam I, these sensors are positioned at midspan. There are 12 sensors, designated from BB1 to BB12, as illustrated in Fig. 2. The locations of the sensors in this beam are listed in Table 2. Measurements are taken between adjacent sensors within each row, and the sensors in the bottom row are not directly paired with those in the top row. Consequently, there are a total of ten sensor pairs, and each sensor pair involves two measurements, swapping the roles of transmitter and receiver between the first and second measurement. Hence, a total of 20 measurements are conducted.

In the second beam, sensors are positioned close to one end of the beam. This beam, denoted Beam II, contains 12 sensors labelled from BS1 to BS12, as shown in Fig. 3. The exact sensor locations are detailed in Table 3. Similar to Beam I, measurements are performed between adjacent sensors within each row, resulting in a total of ten sensor pairs. Therefore, a total of 20 measurements are carried out for Beam II.

The remaining two members are located in a geopolymer concrete slab comprising three beams, with sensors installed in the middle beam (Beam III) and one edge beam (Beam IV). In Beam III, there are 12 sensors labelled from SB1 to SB12, illustrated in Fig. 4. The sensor locations for the middle beam can be found in Table 4. Beam IV incorporates sensors labelled from SS1 to SS10, with their respective locations detailed in Table 5. Similar to the previous setups, measurements are performed between adjacent sensors within each row.

To simplify the formulation, the cross sections shown in Figs. 2(a), 3(a), and 4(a) are approximated as rectangular. As illustrated in Figs. 2(a), 3(a), and 4(a), only small, localized regions near the lower corners of the cross sections are not occupied by concrete. The area of these regions accounts for approximately 1.8% of the total rectangular cross-sectional area in the beam case and 1.2% in the slab case. Given their limited extent, approximating the cross sections as rectangular is considered a valid and sufficiently accurate assumption for the present analysis. For the configurations illustrated in Figs. 2 and 3, L, H, and W are set to 7.35, 0.42, and 1.10, respectively. For the configuration shown in Fig. 4, L, H, and W are taken as 7.35, 0.42, and 3.19, respectively. The tested configurations include differences in both component geometry and sensor location relative to the external boundaries. The approximated width is 1.10 m for the individual beams and 3.19 m for the slab, while the measurement regions include midspan and near-end locations. These variations change the source-receiver-boundary geometry relevant to image-source selection and allow the reduced formulation to be evaluated across several configurations within the same structural system.

3.2. Signal processing and fitting procedure

Since diffusivity and dissipation are functions of frequency, the diffusive properties of body waves must be determined for specific frequency bands. The signal-processing and fitting procedure adopted in this paper consists of three main steps. First, the continuous wavelet transform (CWT) is applied to decompose the original time-domain signal into time–frequency signals at different frequencies. Second, the extracted time–frequency signals are used to calculate the ensemble-averaged energy within selected time-windows, from which the evolution of energy with lapse time is obtained and expressed on a logarithmic scale. Third, the logarithmic energy evolution is fitted using a least-squares procedure to estimate the diffusive properties.

For the signal decomposition, the analytical Morlet wavelet [67,68] is selected as the mother wavelet. The full analysed frequency range is 50 Hz to 1 MHz, with a frequency scale fineness of $2^{1/10}$. For the analysis, the selected frequencies range from 50 kHz to 400 kHz with a 50 kHz interval. For the 50, 100, 150, and 200 kHz bands, the energy is obtained by averaging the CWT coefficients at the central frequency and the two adjacent frequency scales, whereas for the 250, 300, 350, and 400 kHz bands, only the central-frequency scale is used because the corresponding CWT bands are already sufficiently broad.

Once the time–frequency spectrum is obtained, the wave energy is calculated by averaging the squared amplitude within a specific time-window of selected length [41]. The length of the time-window should be at least the reciprocal of the frequency of interest to minimize energy fluctuations caused by waveform oscillations. The centre time of the time-window is taken as the elapsed time t used in the fitting equations. When selecting the beginning and ending time-windows for curve fitting, two factors need to be taken into consideration:

Table 2
Sensor locations in Beam I relative to the coordinates shown in Fig. 2.

Sensor	BB1	BB2	BB3	BB4	BB5	BB6	BB7	BB8	BB9	BB10	BB11	BB12
x [mm]	3070	3315	3560	3815	4070	4325	3070	3315	3560	3815	4070	4325
y [mm]	77	77	77	77	77	77	277	277	277	277	277	277
z [mm]	550	550	550	550	550	550	550	550	550	550	550	550

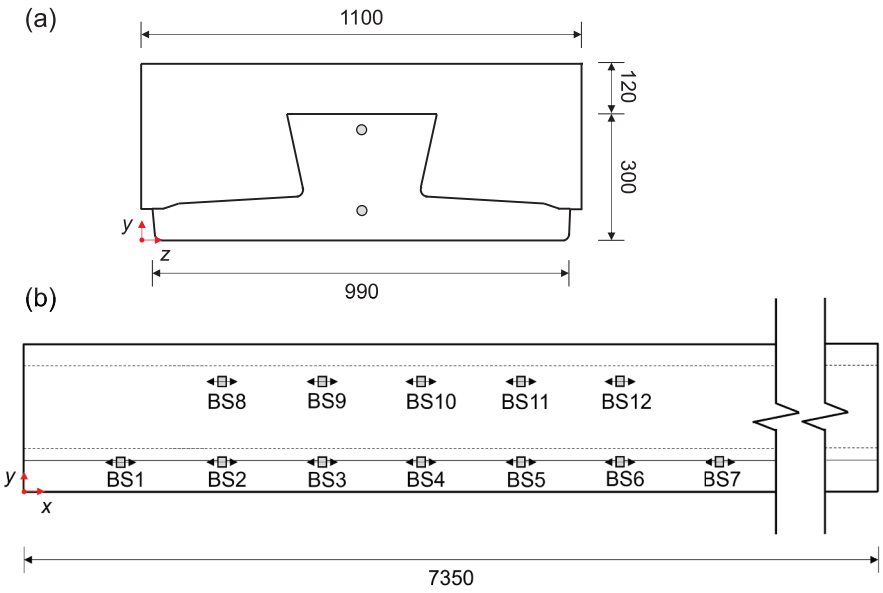


Fig. 3. Dimensions of Beam II and sensor layout (unit: mm; the black arrow on each sensor indicates its polarization direction). (a) Cross-sectional view. (b) Front view.

Table 3
Sensor locations in Beam II relative to the coordinates shown in Fig. 3.

Sensor	BS1	BS2	BS3	BS4	BS5	BS6	BS7	BS8	BS9	BS10	BS11	BS12
x [mm]	260	505	760	1015	1270	1550	1810	505	760	1015	1270	1550
y [mm]	77	77	77	77	77	77	77	277	277	277	277	277
z [mm]	550	550	550	550	550	550	550	550	550	550	550	550

1. The beginning time-window should encompass the first arrival of the wave to smooth the wave energy, particularly to mitigate any sudden increases caused by the ballistic wave (i.e., Fig. 8 in Margerin et al. [46]).
2. The declining trend of the logarithmic energy should exhibit linearity or approximate linearity before the ending time-window. This ensures the reliability of the fitted dissipation, as energy exhibits exponential decay when dissipation predominates.

In practice, the selection of the time-windows should be based on the actual evolution of the logarithmic energy of the measured signal. The determination of the time-window length and location is illustrated in detail in Section 4.1.1.

The logarithm of the resulting windowed, time-dependent energy is fitted to estimate the best-fit diffusivity D, dissipation σ, and initial deposited energy E_0 through unweighted least-squares minimization of the discrepancy between the measured and modelled logarithmic energy evolution. The spread of the extracted diffusivity values across different members and sensor locations is represented using boxplots. This provides a practical characterization of variability, although it should be distinguished from a rigorous uncertainty propagation analysis.

4. Results

Section 4 presents the results in a hierarchical manner. Beam I is first used as the demonstrator to establish the fitting procedure in detail. Specifically, Section 4.1.1 determines the time-windows adopted for energy fitting, Section 4.1.2 evaluates the potential contributions of candidate image sources and defines the reflection cases, and Section 4.1.3 examines the influence of boundary reflections on the fitted diffusivity and dissipation, first for a representative transmitter–receiver pair and then for all sensor pairs in Beam I. After this detailed analysis of Beam I, Section 4.2 extends the comparison to the other members in order to assess the consistency and applicability of the proposed method at the cross-member level.

4.1. Beam I as the demonstrator

4.1.1. Determination of time-windows for logarithmic energy fitting

To demonstrate how the fitting time-windows are determined, the logarithm of the ensemble-averaged energy as a function of lapse time for all 20 transmitter–receiver pairs in Beam I at different frequency components is plotted in Fig. 5. Eight frequency components

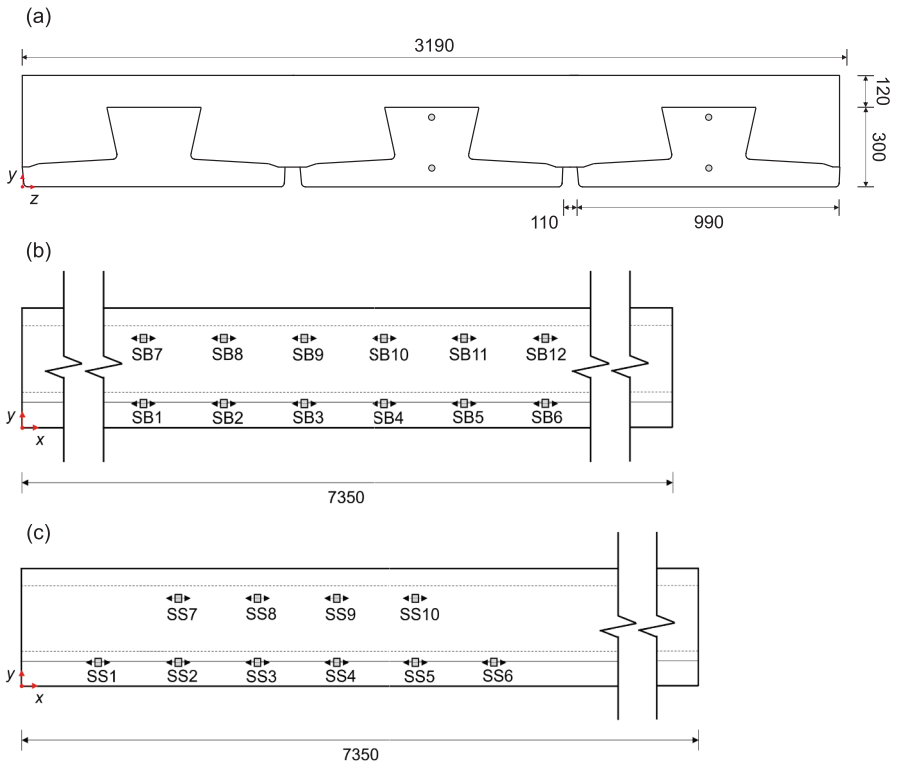


Fig. 4. Dimensions of the geopolymer concrete slab and sensor layouts in Beam III and Beam IV (unit: mm; the black arrow on each sensor indicates its polarization direction). (a) Cross-sectional view of the slab. (b) Front view of Beam III. (c) Front view of Beam IV.

Table 4
Sensor locations in Beam III relative to the coordinates shown in Fig. 4(a) and 4(b).

Sensor	SB1	SB2	SB3	SB4	SB5	SB6	SB7	SB8	SB9	SB10	SB11	SB12
x [mm]	3030	3290	3550	3795	4050	4300	3030	3290	3550	3795	4050	4300
y [mm]	77	77	77	77	77	77	277	277	277	277	277	277
z [mm]	1595	1595	1595	1595	1595	1595	1595	1595	1595	1595	1595	1595

Table 5
Sensor locations in Beam IV relative to the coordinates shown in Fig. 4(a) and 4(c).

Sensor	SS1	SS2	SS3	SS4	SS5	SS6	SS7	SS8	SS9	SS10
x [mm]	275	535	795	1015	1265	1535	535	795	1015	1265
y [mm]	77	77	77	77	77	77	277	277	277	277
z [mm]	2695	2695	2695	2695	2695	2695	2695	2695	2695	2695

ranging from 50 kHz to 400 kHz, with an interval of 50 kHz, are selected. The length of the time-window is initially set as 40 μs (i.e., two times the reciprocal of 50 kHz) for all frequency components, with an overlap of 20 μs between adjacent time-windows. As shown in Fig. 5, the ensemble-averaged energy of all frequency components initially increases rapidly and then decreases. The ascending part primarily corresponds to the spreading of energy in space, while the decreasing part is mainly attributed to dissipation. As the frequency increases, the energy decays at a faster rate. The energy of the components at 350 kHz and 400 kHz reaches the noise level at around 1000 μs. Moreover, the energy in the high-frequency regime, particularly at 350 kHz and 400 kHz, decays rapidly. Nevertheless, before approximately 800 μs, the logarithmic energy evolution still exhibits an approximately linear decreasing trend, which is required for reliable fitting of dissipation. Beyond this stage, the curves gradually approach the noise floor and deviate more noticeably from linearity. Therefore, the ending time-window for curve fitting is chosen so that its centre time remains below 800 μs for all frequency components, thereby retaining the main diffusive decay while avoiding the portion increasingly affected by noise.

As reported by Schubert and Koehler [21], the arrival time of the maximum energy density is dominated by diffusivity, while the subsequent decay is closely related to dissipation. However, as revealed in Fig. 5, using time-windows of equal length to capture the wave energy results in an imbalance of data points between the rising and energy-decaying portions. For example, there will be more

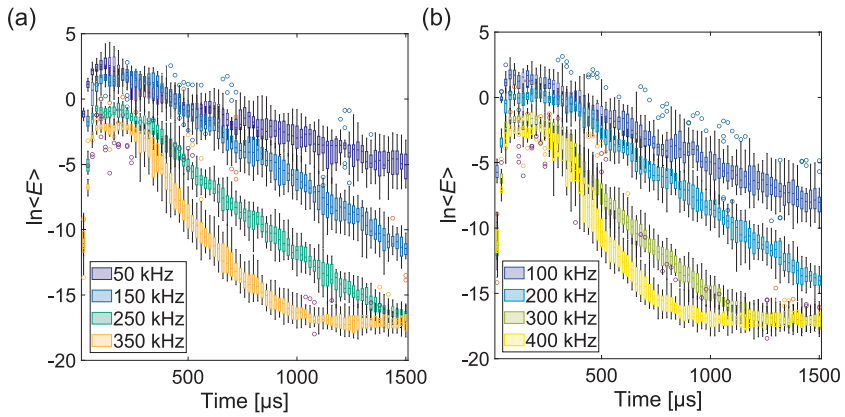


Fig. 5. Boxplots of the ensemble-averaged energy (denoted as ln<E>) evolution with lapse time for all 20 transmitter–receiver pairs in Beam I at different frequency components obtained by CWT: (a) 50, 150, 250, and 350 kHz; (b) 100, 200, 300, and 400 kHz.

data points in the decaying portion (with a negative slope of the logarithm of the energy versus time) between approximately 200 μs and 800 μs, compared to the rising portion (with a positive slope). For small lapse times, the slope of the logarithm of the energy against time is positive and dominated by the term $r^2/4Dt^2$, which is highly related to the diffusivity. For large lapse times, the slope is negative and dominated by the dissipation σ. Therefore, the disparity in data sampling may cause the least-squares fitting to focus more on the decaying portion, where there are more data points, while neglecting the rising portion, which has fewer data points. This can lead to inaccurate estimation of the diffusivity, which is more related to the rising portion.

To balance the sampling of the rising and decaying portions, the signal is divided into two parts: the initial part from 25 μs to 225 μs and the latter part from 225 μs to 725 μs. Choosing 25 μs as the starting time also helps reduce the influence of cross-talk on the obtained energy. The first time-window, starting at 25 μs, has a length of 40 μs. The subsequent 10 time-windows (from the second to the eleventh) also have a length of 40 μs, with each overlapping the previous window by 20 μs. The twelfth time-window, starting at 225 μs, has a length of 100 μs. The subsequent 10 time-windows (from the thirteenth to the twenty-second) have a length of 100 μs and overlap the previous window by 50 μs. In this way, a denser sampling is retained around the early-time rise of the logarithmic energy, where diffusivity plays a dominant role, while a coarser sampling is used for the later decay stage, where dissipation governs the energy evolution.

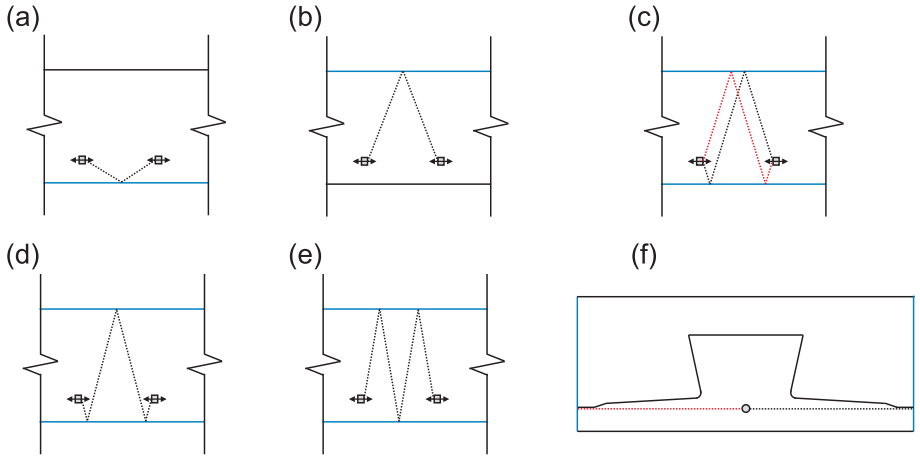


Fig. 6. Illustration of the boundary reflections considered for the sensor pair BB1-BB2. The reflecting boundaries are highlighted in blue. (a) Primary reflection from the bottom surface. (b) Primary reflection from the top surface. (c) Secondary reflections involving the bottom and top surfaces. The red dotted line represents the path reflected first from the top surface and then from the bottom surface, whereas the black dotted line represents the path reflected first from the bottom surface and then from the top surface. (d) Tertiary reflection from the bottom and top surfaces, following a bottom-top–bottom reflection path. (e) Tertiary reflection from the bottom and top surfaces, following a top–bottom-top reflection path. (f) Primary reflections from the front and back surfaces. The red dotted line represents the path reflected from the back surface, whereas the black dotted line represents the path reflected from the front surface. (For interpretation of the references to colour in this figure legend, the reader is referred to the web version of this article.)

4.1.2. Assessment of candidate image sources and definition of reflection cases

Before quantifying the influence of boundary reflections on the fitted diffusive properties, it is first necessary to identify the image sources that may contribute appreciably to the measured energy. In Beam I, the transmitter–receiver pair BB1-BB2 is used as a representative example to illustrate the main reflected paths considered in this section. These include the primary reflections from the bottom and top surfaces, the secondary reflections involving both surfaces, the tertiary reflections associated with repeated reflections between the bottom and top surfaces, and the primary reflections from the front and back surfaces, as shown in Fig. 6. Although BB1-BB2 is used here for illustration, the same classification of reflected paths also applies to the other transmitter–receiver pairs. What varies among sensor pairs is not the type of reflections considered, but their relative contributions, which depend on the sensor locations and their distances to the corresponding boundaries.

To assess the importance of these reflected paths before curve fitting, a preliminary estimate of their relative contributions is made using the factor $\exp\{-[(r')^2-r^2]/(4Dt)\}$. For this estimate, $D = 150$ m^2/s and $t = 800$ μs are adopted as reference values. The selected diffusivity is intentionally taken as a relatively high value representative of the low-frequency regime, in which boundary effects are expected to be more pronounced because the wave energy diffuses faster. The selected lapse time of 800 μs is used as a reference time for screening because it corresponds to the upper limit adopted for the fitting time-windows in Section 4.1.1. It should also be noted that the influence of reflected energy is time-dependent and generally increases with lapse time. Therefore, the values summarized in Table 6 represent estimated contributions at $t = 800$ μs, while the contributions at earlier lapse times are smaller. For this reason, the results in Table 6 are pre-fitting estimates for screening out reflections with negligible contributions. Since the sensor layouts are similar in all members, the same screening logic is generally applicable to all beams. The main exception concerns the side-surface reflections in Beams II and IV, where a limited number of edge sensor pairs are located close to the lateral boundaries and may therefore be affected by such reflections.

On the basis of this preliminary screening, six cases are defined in Section 4.1.3 to quantify the influence of boundary reflections in Beam I:

- Case I: no reflected energy is considered, and the fitting is performed using the diffusion equation for an infinite medium;
- Case II: includes the primary reflections from the bottom and top surfaces (No. 1 and 2 in Table 6);
- Case III: includes the primary and secondary reflections from the bottom and top surfaces (No. 1, 2, and 3 in Table 6);
- Case IV: includes the primary and secondary reflections from the bottom and top surfaces, as well as the primary reflections from the front and back surfaces (No. 1, 2, 3, and 5 in Table 6);
- Case V: includes the primary, secondary, and tertiary reflections from the bottom and top surfaces, as well as the primary reflections from the front and back surfaces (No. 1, 2, 3, 5, 6, and 7 in Table 6);
- Case VI: uses the diffusion equation for a cuboid medium, which theoretically provides the most complete bounded-domain benchmark within the adopted framework among the six cases.

It is important to clarify that, in diffuse elastic-wave studies, diffusivity and dissipation are generally effective transport parameters inferred from measured energy envelopes through diffusion, radiative-transfer, coherent-backscattering, or related model-based approaches. To the best of the authors' knowledge, a generally accepted direct experimental ground truth for elastic-wave diffusivity in strongly scattering heterogeneous solids is not available. Therefore, Case VI should not be interpreted as an independently measured physical reference. Instead, it is used as the most complete cuboid-domain benchmark within the adopted diffusion-equation framework. Accordingly, the relative errors reported in this study quantify the deviation of the reduced image-source formulation from the full bounded-domain diffusion solution, rather than the absolute error with respect to an independent physical ground truth. The purpose of the evaluation is therefore to assess whether the reduced formulation can reproduce the full cuboid-domain benchmark with substantially lower fitting complexity.

4.1.3. Influence of boundary reflections on fitted diffusivity and dissipation

With the fitting time-windows and reflection cases defined above, the influence of boundary reflections on the fitted diffusive

Table 6
Estimated contribution of candidate image sources relative to the direct energy using $\exp\{-[(r')^2-r^2]/(4Dt)\}$ with $D = 150$ m^2/s and $t = 800$ μs.

No.	Boundary reflections	Contribution to the direct energy	
		Sensor pairs on the bottom row	Sensor pairs on the top row
1	Primary reflection from the bottom surface	95.2%	52.8%
2	Primary reflection from the top surface	37.5%	84.3%
3	Secondary reflections from the top and bottom surfaces*	46.0%	46.0%
4	Primary reflection from the side surface (only applicable for selected sensor pairs in Beam II and Beam IV)	33.5% (BS1-BS2)29.4% (SS1-SS2)	4.1% (BS8-BS9)2.9% (SS7-SS8)
5	Primary reflections from the front and back surfaces	16.1%	16.1%
6	Tertiary reflection from the bottom and top surfaces	12.8%	1.8%
7	Tertiary reflection from the top and bottom surfaces	0.8%	7.1%

Note: * For a given transmitter-receiver pair, secondary reflections combine the two second-order reflection sequences involving both the top and bottom surfaces.

properties can now be examined. For the representative transmitter–receiver pair BB1-BB2, the measured logarithmic energy evolution is compared with the fitted curves under four representative reflection cases in Fig. 7. In all four cases, the fitted curves agree well with the experimental data over the selected fitting range, indicating that the estimated diffusivity and dissipation are consistent with the selected diffusion-based fitting framework and that the fitting procedure is reliable for this sensor pair. At the same time, the fitted logarithmic energy evolutions obtained from different cases remain close to each other, even though the underlying fitted equations differ. This observation suggests that fitting quality alone is not sufficient to judge whether boundary reflections have been adequately accounted for, and that a quantitative comparison of the fitted parameters is therefore required.

The corresponding fitted diffusivity and dissipation for BB1-BB2 are summarized in Table 7. For diffusivity, neglecting boundary reflections leads to an underestimation compared with Case VI. In addition, diffusivity decreases with increasing frequency, which is consistent with previous observations reported in the literature [34]. The influence of boundary reflections is frequency dependent: it is minor at high frequencies but becomes substantial at low frequencies, especially at 50 kHz. For example, the fitted diffusivity at 50 kHz increases from 93.0 m^2/s in Case I to 101.5 m^2/s in Case VI. However, once the primary reflections from the top and bottom surfaces and the secondary reflections between these two surfaces are included (Case III), the improvement becomes nearly saturated. Compared with Case III, Cases IV and V provide only marginal additional changes in diffusivity. A similar trend can be observed for dissipation. Ignoring boundary reflections also results in an underestimation of dissipation, while dissipation increases with frequency, again in agreement with previous studies [34]. Compared with diffusivity, the fitted dissipation is more sensitive to the treatment of reflected energy, which is evident at low frequencies. At 50 kHz, the fitted dissipation increases from 300 s^{-1} in Case I to 806 s^{-1} in Case VI. Nevertheless, similar to diffusivity, the additional reflections included in Cases IV and V only lead to limited improvements relative to Case III, indicating that the dominant boundary-reflection effects have already been captured in Case III.

These trends are quantified further in Fig. 8, where the relative errors of diffusivity and dissipation are evaluated with respect to Case VI, which is regarded here as the benchmark within the adopted diffusion-equation framework. Please note that the reported relative errors are described as deviations from the full cuboid-domain benchmark, or model-reduction errors, rather than absolute errors with respect to a ground truth. In Case I, where no reflected energy is considered, the errors are the largest and are particularly pronounced at low frequencies. After the primary reflections from the top and bottom surfaces are included in Case II, the errors at

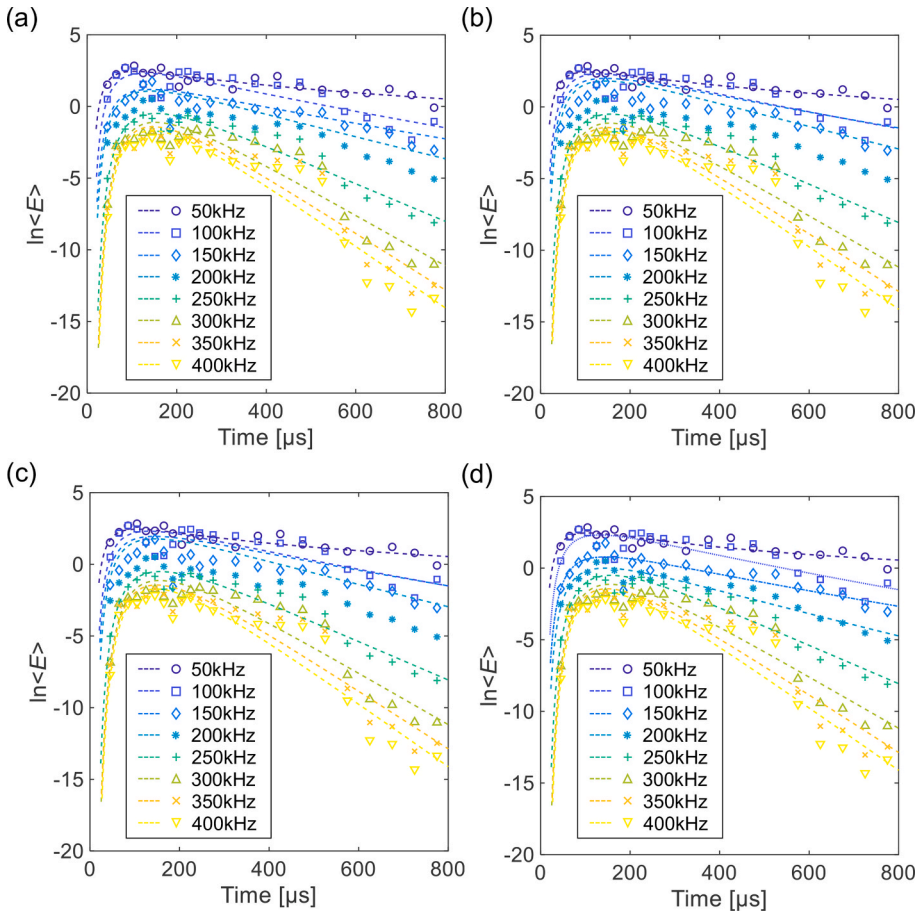


Fig. 7. Comparison between the measured logarithmic energy evolution and the fitted diffusion curves for the transmitter–receiver pair BB1-BB2 in Beam I under different reflection cases: (a) Case I, (b) Case II, (c) Case III, and (d) Case VI.

Table 7
Fitted diffusivity and dissipation for the transmitter–receiver pair BB1-BB2 in Beam I under different reflection cases.

Frequency [kHz]	Diffusivity D [m^2/s]					
	Case I	Case II	Case III	Case IV	Case V	Case VI
50	93.0	104.3	103.2	102.7	102.3	101.5
100	57.6	61.8	61.3	61.3	61.2	61.2
150	51.9	56.0	55.8	55.8	55.8	55.8
200	44.4	47.2	47.2	47.2	47.2	47.2
250	29.2	30.1	30.1	30.1	30.1	30.1
300	24.4	24.9	24.9	24.9	24.9	24.9
350	24.0	24.5	24.5	24.5	24.5	24.5
400	22.8	23.2	23.2	23.2	23.2	23.2

Frequency [kHz]	Dissipation σ [s^{-1}]					
	Case I	Case II	Case III	Case IV	Case V	Case VI
50	300	550	705	736	765	806
100	4108	4402	4461	4465	4472	4477
150	3839	4092	4125	4127	4131	4133
200	6205	6505	6523	6523	6525	6525
250	11,998	12,452	12,454	12,454	12,454	12,454
300	16,661	17,188	17,189	17,189	17,189	17,189
350	18,869	19,402	19,402	19,402	19,402	19,402
400	20,629	21,176	21,176	21,176	21,176	21,176

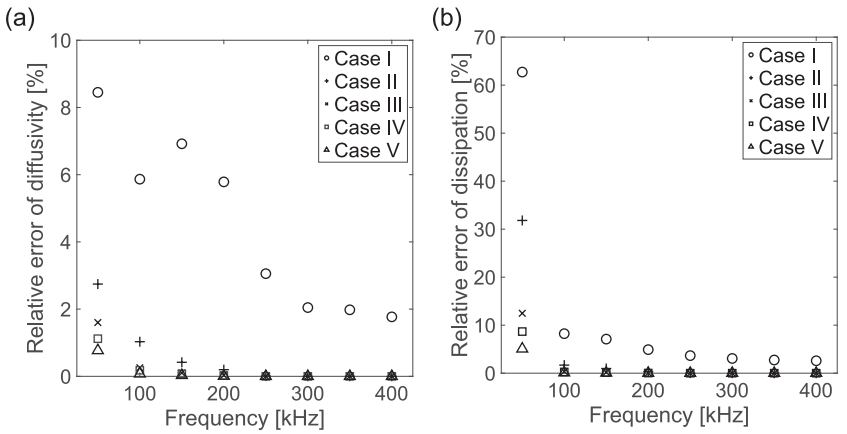


Fig. 8. Relative errors of the fitted (a) diffusivity and (b) dissipation for different reflection cases with respect to Case VI shown in Table 7.

medium and high frequencies are reduced. However, the errors at 50 kHz and 100 kHz remain significant, indicating that first-order reflections alone are insufficient to account for the low-frequency boundary effect. When the secondary reflections between the top and bottom surfaces are further included in Case III, the low-frequency error is reduced markedly, especially for dissipation. At 50 kHz, the relative error decreases to 1.7% for diffusivity and 12.5% for dissipation in Case III. Beyond this point, the improvements obtained in Cases IV and V become much smaller than the improvement from Case II to Case III. In other words, the results enter a near-plateau regime after Case III, suggesting that the inclusion of additional image sources beyond the top–bottom secondary reflections provides only limited gains in accuracy for this sensor pair.

The pair-level analysis above establishes the main trends for a representative measurement. The analysis is next extended to all transmitter–receiver pairs in Beam I to examine whether these trends persist at the member level. All computations were performed in MATLAB R2024b on a laptop equipped with an Intel Core i7-14650HX processor. Nonlinear least-squares fitting was performed with the tolerance option set to 10^{-10}. The amplitude parameter, diffusivity, and dissipation were constrained to be positive, with no upper bounds. Cases I-V evaluated Eq. (6) with the corresponding image-source contributions using array operations. Case VI evaluated Eq. (3) as the product of three one-dimensional eigenfunction series, each retaining 500 nonzero modes. Two implementations of Case VI were compared: a nested-loop implementation over time points and mode indices (VI-loop), and a vectorized implementation using matrix operations with geometry-dependent coefficients precomputed and reused during fitting (VI-vectorized). Both implementations used the same analytical expression and series truncation.

Fig. 9(a) compares the total nonlinear-fitting times. For each case and implementation, one run comprised 160 fits covering 20 directed transmitter–receiver measurements and eight frequency bands. This complete workload was repeated 20 times, and the inset

reports the mean runtimes and standard deviations. The mean fitting times for Cases I-V ranged from 1.98 to 2.23 s, compared with 127.93 s for VI-loop and 6.24 s for VI-vectorized. The substantial reduction in the runtime of Case VI demonstrates the influence of numerical implementation on the computational comparison. Relative to the vectorized Case VI implementation, Cases I-V required approximately 66% less fitting time. The reduced image-source formulations therefore retained a computational advantage for the workload, implementations, and truncation settings examined.

Fig. 9(b) presents the coefficient of determination R^2 between the measured and fitted logarithmic energy evolution for all transmitter–receiver pairs in Beam I, while the corresponding mean values and standard deviations are summarized in Table 8. This index provides a quantitative measure of the agreement between the fitted curves and the original energy evolution, and can therefore be regarded as a statistical extension of the pair-level comparison shown previously in Fig. 7. Two observations are noteworthy. First,

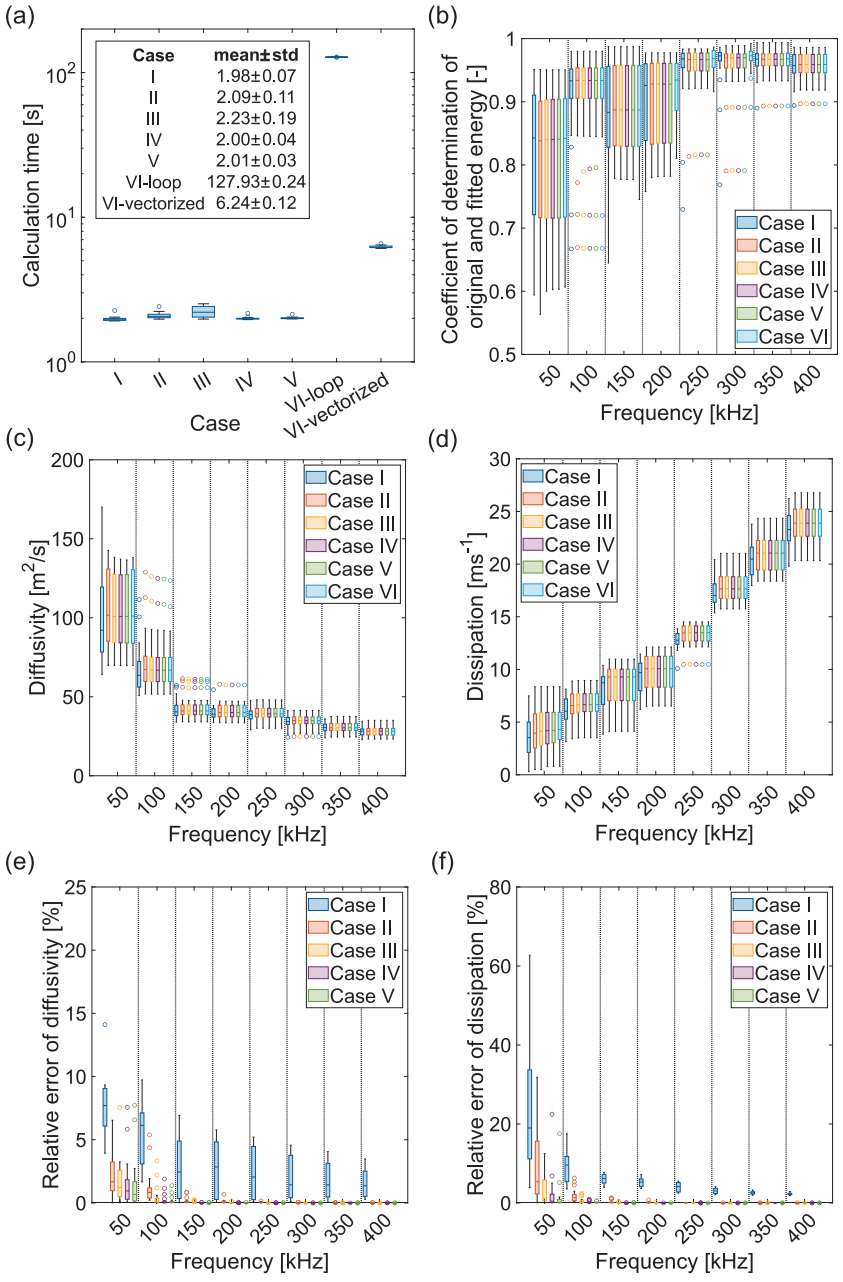


Fig. 9. Comparison of computational cost, fitting quality, and extracted diffusive properties for all transmitter–receiver pairs in Beam I under different reflection cases: (a) calculation time over 20 repeated runs, each comprising 160 fits; (b) coefficient of determination R^2 between the measured and fitted logarithmic energy evolution; (c) diffusivity; (d) dissipation; (e) relative error of diffusivity with respect to Case VI; and (f) relative error of dissipation with respect to Case VI.

the six reflection cases do not show significant differences in R^2, indicating that the overall goodness of fit remains similar even when different numbers of image sources are considered. Second, the variability of R^2 strongly depends on frequency. At 50 kHz, the coefficient of determination shows the largest scatter among sensor pairs. The fluctuations remain noticeable at 100–200 kHz, but are significantly smaller than those at 50 kHz. In contrast, for frequencies from 250 kHz to 400 kHz, R^2 generally remains at a high level with relatively small variability.

The fitted diffusivity and dissipation obtained from all transmitter–receiver pairs in Beam I are shown in Fig. 9(c) and (d), respectively. The overall trends are consistent with those observed previously for the BB1-BB2 pair and with the numerical values listed in Table 7. Diffusivity decreases with increasing frequency, whereas dissipation increases with frequency. Moreover, the influence of boundary reflections is again most pronounced at low frequencies, especially at 50 kHz, and becomes progressively less important as frequency increases. These results confirm that the frequency dependence and the role of reflected energy identified from the representative sensor pair are not isolated features, but are also observed at the member level.

The relative errors of diffusivity and dissipation for all transmitter–receiver pairs in Beam I are further presented in Fig. 9(e) and (f), with the corresponding mean values and standard deviations summarized in Table 9. Here, the relative errors are evaluated with respect to Case VI, which is taken as the full cuboid-domain benchmark. Similar to the pair-level results shown in Fig. 8, the largest errors occur in Case I, where no reflected energy is considered. The errors are especially significant at low frequencies. After the primary reflections from the top and bottom surfaces are included in Case II, the errors are reduced. A further marked improvement is achieved in Case III when the secondary reflections between the top and bottom surfaces are included. Beyond Case III, the reductions in relative error from Cases IV and V become much smaller. This member-level result further confirms the conclusion drawn from the BB1-BB2 pair, namely that considering more reflections in Cases IV and V does not lead to a substantial improvement in the fitted results. In addition, the mean relative errors in Case III are already below 2% for both diffusivity and dissipation, suggesting that this case provides close agreement with the full bounded-domain benchmark while avoiding the much higher computational cost associated with more complete formulations.

4.2. Cross-member comparison and benchmark consistency of fitted properties

In Section 4.1, Beam I was used to establish and compare the candidate reflection configurations. The reflection cases I, III, V and VI selected from this analysis were subsequently evaluated in Beams II-IV using the same reference diffusivity of 150 m^2/s, lapse time of 800 μs, and signal-processing settings. The relevant image-source locations and contributions were calculated separately from the geometry and sensor coordinates of each member. For the edge transmitter–receiver pairs in Beams II and IV, the reflected energy from the side surface is additionally included in Case III because the corresponding sensors are located close to the lateral boundary.

The fitted diffusivity obtained for Beams II, III, and IV is compared in Fig. 10 together with its relative error under Cases I, III, V, and VI. In all three beams, diffusivity decreases with increasing frequency, which is consistent with the observations made for Beam I. A systematic underestimation can again be observed in Case I, especially at low frequencies. The diffusivity distributions obtained in Cases III, V, and VI are generally close to each other, showing that the dominant boundary-reflection effects have already been captured in Case III. The corresponding relative errors shown in Fig. 10(b), (d), and (f) further confirm this trend. Compared with Case I, the errors in Case III are markedly reduced for all three beams, particularly at 50 and 100 kHz. The additional reflections included in Case V lead only to limited further improvement relative to Case III. This is consistent with the conclusion drawn from Beam I.

A similar comparison for dissipation is given in Fig. 11. Similar to Beam I, dissipation increases with increasing frequency in all three beams. The fitted dissipation in Case I is consistently lower than that in Cases III, V, and VI, again demonstrating that neglecting reflected energy leads to an underestimation of the diffusive properties. Compared with diffusivity, the dissipation remains more sensitive to the treatment of reflected energy, particularly at low frequencies. The relative-error plots in Fig. 11(b), (d), and (f) show that the largest discrepancies are again associated with Case I, while Case III reduces the error substantially across all beams. Together with the diffusivity results, these observations support the use of Case III as a practical and sufficiently accurate approximation.

To quantify this agreement, the mean values and standard deviations of the relative errors are summarized in Table 10 for Case III using Case VI as the benchmark. For all four beams, the mean relative errors of both diffusivity and dissipation remain below 2% over the entire analysed frequency range. Considering the estimated reflection contributions in Table 6 together with the benchmark

Table 8
Mean value ± standard deviation of the coefficient of determination R^2 between the measured and fitted logarithmic energy evolution for all transmitter–receiver pairs in Beam I under different reflection cases. The mean value and standard deviation are calculated after excluding outliers identified from the data distribution with respect to the median.

Frequency [kHz]	Mean value ± standard deviation of the coefficient of determination [-]					
	Case I	Case II	Case III	Case IV	Case V	Case VI
50	0.819 ± 0.107	0.809 ± 0.117	0.813 ± 0.112	0.812 ± 0.113	0.813 ± 0.112	0.818 ± 0.105
100	0.941 ± 0.021	0.937 ± 0.031	0.937 ± 0.031	0.937 ± 0.031	0.937 ± 0.031	0.937 ± 0.031
150	0.879 ± 0.088	0.894 ± 0.070	0.893 ± 0.070	0.893 ± 0.070	0.893 ± 0.070	0.886 ± 0.076
200	0.907 ± 0.067	0.915 ± 0.063	0.915 ± 0.062	0.915 ± 0.062	0.915 ± 0.062	0.918 ± 0.055
250	0.966 ± 0.016	0.963 ± 0.019	0.963 ± 0.018	0.963 ± 0.018	0.963 ± 0.018	0.964 ± 0.021
300	0.974 ± 0.008	0.967 ± 0.015	0.967 ± 0.015	0.967 ± 0.015	0.967 ± 0.015	0.974 ± 0.012
350	0.966 ± 0.015	0.967 ± 0.014	0.967 ± 0.014	0.967 ± 0.014	0.967 ± 0.014	0.967 ± 0.015
400	0.959 ± 0.019	0.957 ± 0.023	0.957 ± 0.023	0.957 ± 0.023	0.957 ± 0.023	0.957 ± 0.023

Table 9
Mean value ± standard deviation of the relative errors of diffusivity and dissipation for all transmitter–receiver pairs in Beam I under different reflection cases, using Case VI as the benchmark. The mean value and standard deviation are calculated after excluding outliers identified from the data distribution with respect to the median.

Frequency [kHz]	Mean value ± standard deviation of the relative errors of diffusivity [%]				
	Case I	Case II	Case III	Case IV	Case V
50	7.569 ± 2.181	2.092 ± 1.748	1.364 ± 1.071	0.968 ± 0.905	0.816 ± 0.875
100	5.447 ± 2.447	0.767 ± 0.461	0.169 ± 0.159	0.028 ± 0.025	0.042 ± 0.016
150	2.779 ± 2.543	0.075 ± 0.046	0.006 ± 0.007	0.002 ± 6.9e-4	0.006 ± 0.004
200	2.648 ± 2.332	0.086 ± 0.065	0.007 ± 0.008	0.002 ± 5.9e-4	0.007 ± 0.006
250	2.440 ± 2.160	0.038 ± 0.030	0.002 ± 0.002	0.001 ± 7.3e-4	0.003 ± 0.002
300	2.002 ± 1.741	0.010 ± 0.008	4.2e-4 ± 4.2e-4	2.6e-4 ± 2.3e-4	5.1e-4 ± 4.8e-4
350	1.767 ± 1.393	0.003 ± 0.002	1.6e-4 ± 1.3e-4	1.9e-4 ± 1.3e-4	2.4e-4 ± 1.9e-4
400	1.567 ± 1.093	0.002 ± 0.002	1.3e-4 ± 1.2e-4	2.5e-4 ± 2.0e-4	3.1e-4 ± 2.5e-4
Frequency [kHz]	Mean value ± standard deviation of the relative errors of dissipation [%]				
	Case I	Case II	Case III	Case IV	Case V
50	19.655 ± 11.631	7.798 ± 7.993	1.497 ± 1.639	0.474 ± 0.542	0.196 ± 0.197
100	9.264 ± 4.104	1.344 ± 1.090	0.243 ± 0.240	0.043 ± 0.039	0.080 ± 0.050
150	6.087 ± 1.292	0.105 ± 0.062	0.008 ± 0.008	0.003 ± 7.7e-4	0.008 ± 0.005
200	5.233 ± 1.043	0.111 ± 0.088	0.006 ± 0.007	0.003 ± 0.001	0.009 ± 0.008
250	4.026 ± 1.200	0.051 ± 0.032	0.003 ± 0.002	0.002 ± 7.4e-4	0.003 ± 0.002
300	3.050 ± 0.676	0.011 ± 0.008	1.4e-4 ± 1.6e-4	3.4e-4 ± 3.1e-4	5.7e-4 ± 5.3e-4
350	2.555 ± 0.364	0.003 ± 0.003	8.9e-5 ± 8.6e-5	1.2e-4 ± 1.2e-5	1.1e-4 ± 1.2e-5
400	2.229 ± 0.225	0.002 ± 0.002	8.6e-5 ± 8.3e-5	1.1e-4 ± 9.2e-5	1.4e-4 ± 1.2e-5

comparisons across all four members, a contribution level of approximately 30% is suggested as an empirical reference for reflection screening in similar configurations.

The final fitted diffusivity and dissipation obtained in Case III are summarized for all four beams in Table 11. Even for members made of the same material, the extracted diffusivity still shows a noticeable degree of variation among different beams at both low and high frequencies. This suggests that diffusivity is spatially sensitive and may fluctuate with local heterogeneity, sensor location, and wave-propagation path within the concrete. Compared with diffusivity, the dissipation values also vary among beams. Taken together, these results indicate that the proposed fitting method can provide consistent frequency-dependent diffusive properties across different members, while also revealing the inherent spatial variability of the extracted parameters in concrete.

5. Discussion

5.1. Sensitivity and practical interpretation of the image-source selection criterion

The sensitivity of the image-source selection criterion to the assumed diffusivity and lapse time is further examined in this section. The estimated contribution ratio of an image source is given by $\exp\{-[(r')^2-r^2]/(4Dt)\}$. Therefore, the contribution ratio is controlled by three factors: the diffusivity D, the lapse time t, and the effective distance penalty $r_p^2=(r')^2-r^2$. Here, r and r' denote the receiver-to-real-source and receiver-to-image-source distances, respectively. The contribution ratio increases with increasing D and t, and decreases as r_p increases for fixed D and t. For the 30% reference level examined in this section, the threshold condition can be written as $\exp[-r_p^2/(4Dt)] = 0.3$, which gives the critical distance-penalty parameter $r_{p_cri} = \mathrm{sqrt}(-4 \times \ln 0.3 \times Dt)$. An image source with $r_p < r_{p_cri}$ is expected to contribute more than 30% of the direct energy. Fig. 12(a) shows the variation of r_{p_cri} with D and t. The diffusivity is varied from 10 to 100 m^2/s, covering the range from high-frequency components with relatively low diffusivity to low-frequency components with relatively high diffusivity. The lapse time is varied from 200 to 1000 μs to cover the main time range relevant to the energy fitting and the late-time regime where reflected energy is more likely to contribute. As shown in this figure, r_{p_cri} increases with both D and t. This means that image sources with a larger distance penalty may still exceed the 30% contribution threshold when the diffusivity is large or the lapse time is long. If a smaller diffusivity corresponding to high-frequency components is used, r_{p_cri} decreases and fewer image sources may exceed the 30% threshold. This behaviour is consistent with the fitted results, which show that boundary effects are stronger at low frequencies and weaker at high frequencies. The choice of $D = 150$ m^2/s and $t = 800$ μs in the preliminary screening is therefore interpreted as a conservative low-frequency and late-time condition, rather than as an assumed final value of diffusivity. It is used to avoid excluding image sources that may become important under the conditions where boundary reflections are most pronounced. Therefore, the suggested 30% criterion should be regarded as a practical screening criterion for the tested members, used to identify the dominant image sources under conservative conditions.

Although complete bounded-domain solutions are theoretically available, their availability does not resolve the practical model-selection problem encountered in diffuse-wave measurements: for a given diffusivity, fitting window, and source-receiver-boundary geometry, it remains unclear whether an energy-contribution criterion can reliably identify such conditions. This question cannot be answered unambiguously using the experimental data alone because no generally accepted independent procedure is currently

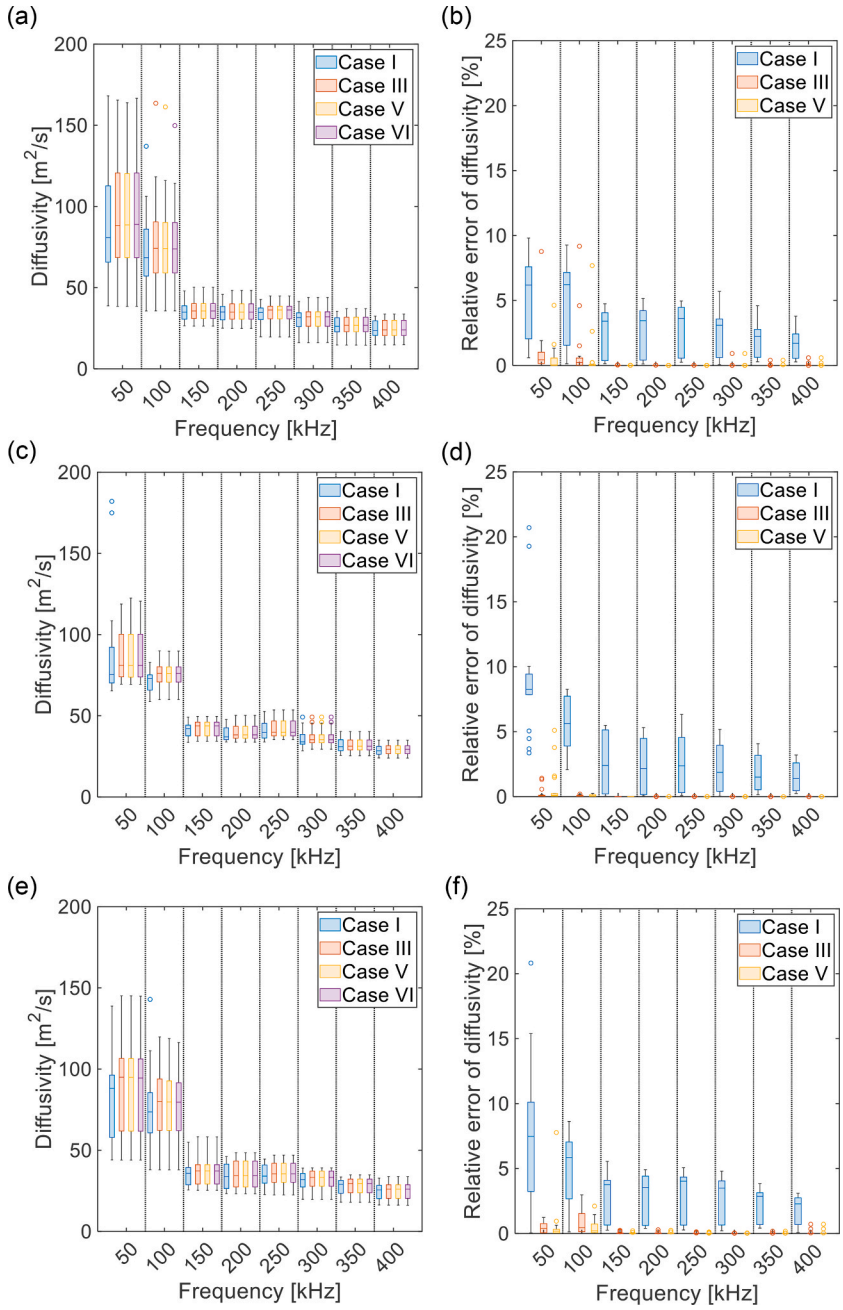


Fig. 10. Comparison of the fitted diffusivity and its relative error with respect to Case VI for all transmitter–receiver pairs in Beams II, III, and IV under Cases I, III, V, and VI: (a,b) Beam II; (c,d) Beam III; (e,f) Beam IV.

available for directly measuring the diffusivity and dissipation of the tested concrete members. A controlled known-parameter numerical analysis was therefore introduced with three specific objectives. First, by generating energy curves from prescribed diffusivity and dissipation values, the parameter-retrieval errors associated with different fitting formulations can be quantified against known numerical inputs rather than against another fitted result. Second, systematic variation of diffusivity, lapse time, and source-to-boundary distance enables examination of whether the 30% contribution criterion can act as a conservative screening indicator for conditions susceptible to substantial boundary-induced errors. Third, comparison between the infinite-medium and threshold-guided formulations quantifies the reduction in parameter-estimation error achieved by retaining reflected energy only when its estimated contribution is significant.

The controlled analysis was performed using the full cuboid-domain solution. The cuboid dimensions were set to $L_x = 100$ m and $L_y = L_z = 200$ m. The source was positioned at distances ranging from 0.05 to 1.00 m from the $x = 0$ boundary, with an increment of

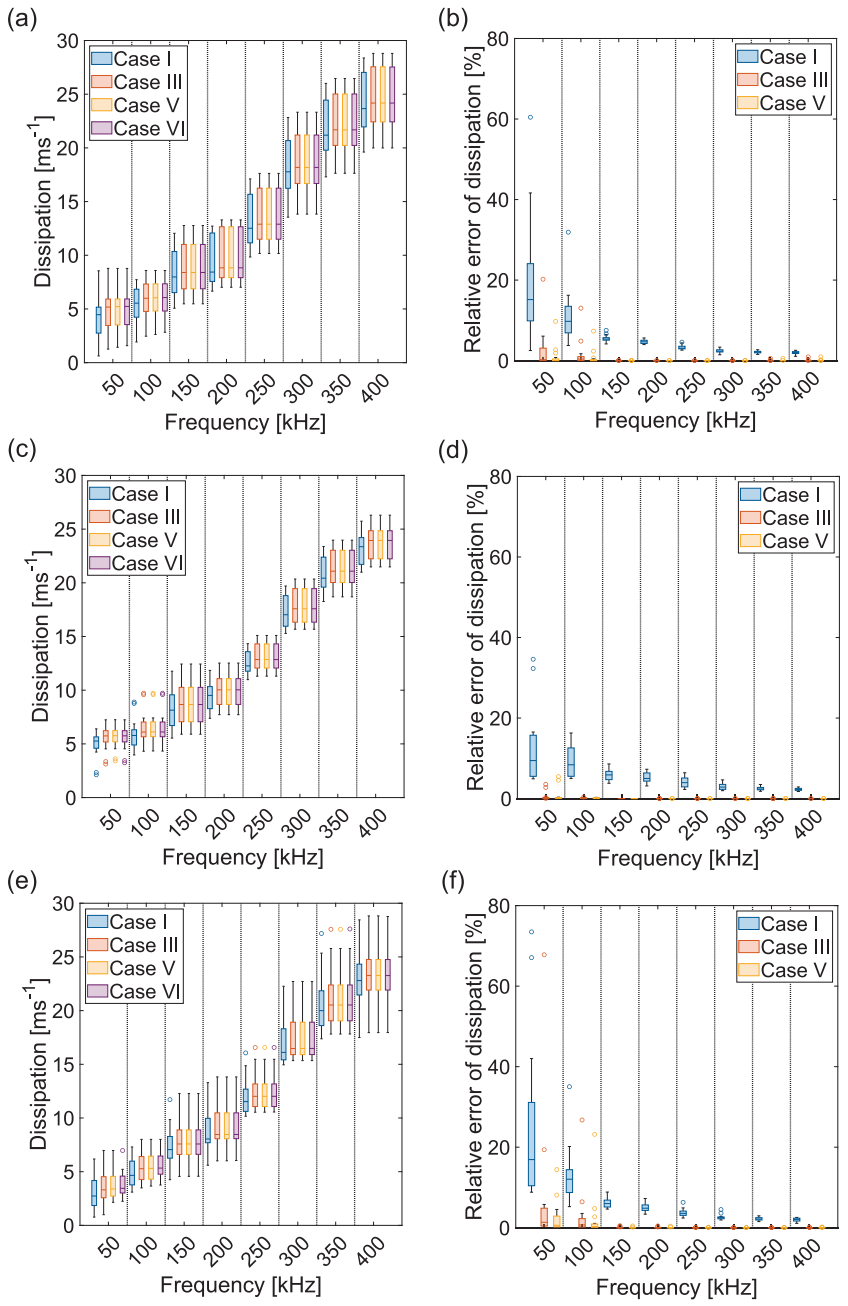


Fig. 11. Comparison of the fitted dissipation and its relative error with respect to Case VI for all transmitter–receiver pairs in Beams II, III, and IV under Cases I, III, V, and VI: (a,b) Beam II; (c,d) Beam III; (e,f) Beam IV.

0.05 m, while the receiver was placed 0.25 m farther from the same boundary. Both the source and receiver were located at the centres of the other two dimensions with $y = z = 100$ m. The large dimensions in the remaining directions were selected to make the influence of the other boundaries negligible, thereby isolating the effect of the nearest planar boundary. Ten prescribed transport-parameter pairs were considered. The diffusivity increased from 10 to 100 m^2/s in increments of 10 m^2/s, while the corresponding dissipation decreased from 31,000 to 4000 s^{-1} in increments of 3000 s^{-1}. The synthetic energy curves covered lapse times from 65 to 1000 μs. In this controlled analysis, the diffusivity prescribed for generating each synthetic energy curve was also used solely to evaluate the image-source contribution index, and the contribution was calculated at the maximum lapse time of the synthetic fitting window, 1000 μs. This choice was intentional because the objective was to assess the intrinsic screening performance of the 30% contribution level over different known diffusivities and source-to-boundary distances. Since the estimated contribution increases monotonically with lapse time, evaluation gives the maximum contribution of each image source within the fitting window and therefore provides a

Table 10
Mean value ± standard deviation of the relative errors of diffusivity and dissipation for all transmitter–receiver pairs in Beams I, II, III, and IV in Case III, using Case VI as the benchmark. The mean value and standard deviation are calculated after excluding outliers identified from the data distribution with respect to the median.

Frequency [kHz]	Relative error of diffusivity [%]			
	Beam I	Beam II	Beam III	Beam IV
50	1.364 ± 1.071	0.568 ± 0.573	0.066 ± 0.043	0.411 ± 0.403
100	0.169 ± 0.159	0.216 ± 0.227	0.069 ± 0.051	0.459 ± 0.574
150	0.006 ± 0.007	2.7e-4 ± 2.8e-4	0.004 ± 0.004	0.005 ± 0.007
200	0.007 ± 0.008	0.002 ± 0.002	7.8e-4 ± 7.8e-4	0.006 ± 0.010
250	0.002 ± 0.002	8.0e-4 ± 6.9e-4	4.4e-4 ± 5.3e-4	0.002 ± 0.002
300	4.2e-4 ± 4.2e-4	1.6e-4 ± 1.8e-4	7.6e-5 ± 6.2e-5	4.7e-4 ± 5.7e-4
350	1.6e-4 ± 1.3e-4	1.1e-4 ± 1.5e-4	6.6e-5 ± 4.9e-5	3.1e-4 ± 2.6e-4
400	1.3e-4 ± 1.2e-4	5.1e-5 ± 6.9e-5	9.5e-5 ± 7.9e-5	1.3e-4 ± 1.3e-4
Frequency [kHz]	Relative error of dissipation [%]			
	Beam I	Beam II	Beam III	Beam IV
50	1.497 ± 1.639	0.121 ± 0.143	0.129 ± 0.045	1.976 ± 2.036
100	0.243 ± 0.240	0.475 ± 0.556	0.111 ± 0.083	0.723 ± 0.802
150	0.008 ± 0.008	4.9e-4 ± 4.7e-4	0.006 ± 0.006	0.008 ± 0.010
200	0.006 ± 0.007	0.002 ± 0.003	0.001 ± 0.001	0.011 ± 0.015
250	0.003 ± 0.002	0.001 ± 0.001	7.3e-4 ± 7.5e-4	0.003 ± 0.004
300	1.4e-4 ± 1.6e-4	1.4e-4 ± 1.8e-4	1.5e-4 ± 1.8e-4	8.3e-4 ± 7.9e-4
350	8.9e-5 ± 8.6e-5	2.8e-5 ± 3.2e-5	2.1e-5 ± 1.6e-5	2.4e-4 ± 2.6e-4
400	8.6e-5 ± 8.3e-5	2.7e-5 ± 4.6e-5	4.0e-5 ± 3.8e-5	7.0e-5 ± 5.4e-5

Table 11
Mean value ± standard deviation of the diffusivity and dissipation obtained in Case III for all transmitter–receiver pairs in Beams I, II, III, and IV. The mean value and standard deviation are calculated after excluding outliers identified from the data distribution with respect to the median.

Frequency [kHz]	Diffusivity D [m^2/s]			
	Beam I	Beam II	Beam III	Beam IV
50	101.48 ± 23.06	93.65 ± 35.36	84.55 ± 14.99	85.15 ± 28.49
100	66.76 ± 10.74	74.53 ± 23.83	74.99 ± 7.71	76.01 ± 21.15
150	40.54 ± 3.70	36.48 ± 7.55	42.34 ± 5.01	37.38 ± 10.06
200	40.32 ± 3.94	35.40 ± 6.50	39.74 ± 4.52	35.66 ± 9.14
250	39.70 ± 4.25	37.27 ± 4.15	42.01 ± 5.92	35.92 ± 6.93
300	34.83 ± 3.75	31.05 ± 7.25	34.39 ± 2.60	32.06 ± 6.22
350	30.69 ± 3.45	27.27 ± 6.18	31.86 ± 4.27	27.90 ± 5.57
400	28.24 ± 3.12	24.80 ± 5.58	29.19 ± 3.33	25.14 ± 5.39
Frequency [kHz]	Dissipation σ [s^{-1}]			
	Beam I	Beam II	Beam III	Beam IV
50	4300 ± 2178	4774 ± 1971	5858 ± 705	3576 ± 1479
100	6644 ± 1460	5999 ± 1648	6102 ± 825	5460 ± 1350
150	8720 ± 1706	8908 ± 2375	8707 ± 2004	7723 ± 1971
200	9751 ± 1813	9977 ± 2330	10032 ± 1516	8910 ± 1802
250	13289 ± 1003	13687 ± 2537	13224 ± 1278	12503 ± 1822
300	17741 ± 1349	18734 ± 2762	17881 ± 1558	16837 ± 1432
350	20979 ± 1718	22290 ± 2779	21245 ± 1662	21099 ± 2785
400	23842 ± 1892	24688 ± 2795	23844 ± 1516	23208 ± 2521

conservative time-based screening condition. The prescribed diffusivity was used only for this controlled criterion-level assessment and should not be interpreted as the operational procedure for experimental measurements, in which diffusivity is unknown and the screening is performed using a conservative expected diffusivity range. Because of the large domain dimensions and short lapse times, the modal series shown in Eq. (3) converges relatively slowly at early lapse times. Therefore, 10,000 non-zero eigenmodes were retained in each one-dimensional modal series to ensure adequate convergence of the synthetic energy curves. Because the input transport parameters were prescribed before generating the energy curves, they provide known numerical reference values against which the fitted parameters can be evaluated.

Fig. 12(b) shows that neglecting the reflected energy produces a strongly distance-dependent bias in the diffusivity recovered using the infinite-medium solution. For the relatively high-diffusivity cases, the fitted diffusivity initially underestimates the prescribed value near the boundary, subsequently crosses and exceeds the prescribed value, and finally decreases towards it as the source-to-

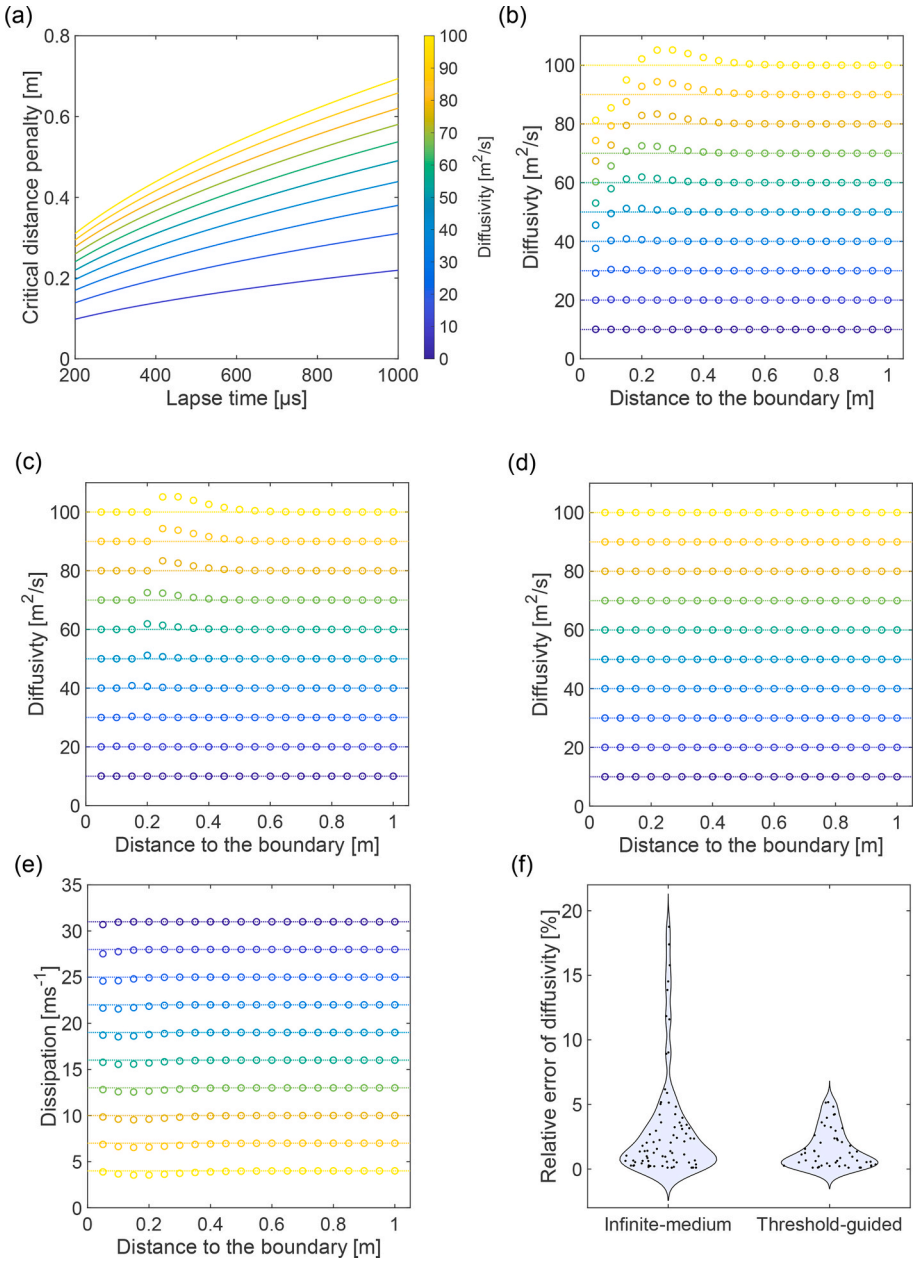


Fig. 12. Analytical basis and controlled known-parameter numerical assessment of the 30% image-source contribution criterion. (a) Critical effective distance penalty corresponding to an image-source contribution of 30% as a function of diffusivity and lapse time. (b-d) Diffusivity recovered from synthetic bounded-domain energy curves using (b) the infinite-medium solution, (c) the threshold-guided fitting scheme, and (d) the single-boundary image-source formulation. In the threshold-guided scheme, the infinite-medium result is retained when the estimated image-source contribution is below 30%, whereas the reflection-inclusive result is adopted when the contribution exceeds 30%. (e) Dissipation coefficients recovered using the infinite-medium solution. The horizontal dotted lines in (b-e) denote the prescribed parameter values, and the circles denote the corresponding fitted values. (f) Distributions of the non-negligible relative diffusivity errors (>0.1%) obtained using the infinite-medium and threshold-guided fitting schemes. Cases with errors at or below 0.1% were excluded from this visualization to improve the distinction between the two distributions. The black dots represent individual retained cases, and the violin envelopes represent their kernel-density estimates.

boundary distance increases. Therefore, the agreement observed at an isolated crossing point results from a temporary cancellation of the signed fitting bias and should not be interpreted as robust parameter recovery by the infinite-medium model. Another noteworthy observation is that the boundary-induced fitting bias is relatively small at low diffusivities, which generally correspond to higher-frequency components, but becomes progressively more pronounced as diffusivity increases towards the low-frequency regime (below 150 kHz in the present measurements). This observation helps clarify the scope of the recent work by Kim [69], which reported

that the peak arrival time of diffuse energy is independent of domain geometry, including its size, shape, and boundary conditions. The prescribed diffusivities considered in that study were 7, 10, and 15 m^2/s. The weak boundary influence observed at the lower diffusivities in Fig. 12(b) is consistent with the conditions under which Kim obtained nearly coincident peak-arrival times. However, at the higher diffusivities representative of the low-frequency regime in the present numerical cases, omitting the boundary contribution can produce non-negligible and geometry-dependent errors in the fitted diffusivity. Accordingly, Kim's conclusion should be interpreted as applying primarily to the low-diffusivity conditions representative of higher-frequency signals, whereas it may not remain valid for frequencies below approximately 150 kHz in the present concrete members; under such low-frequency conditions, the contribution-based procedure proposed in this study is recommended to assess the significance of reflected energy before selecting the appropriate fitting formulation.

The threshold-guided results are presented in Fig. 12(c). When the estimated image-source contribution exceeds 30%, the reflection-inclusive result is adopted; otherwise, the computationally simpler infinite-medium result is retained. This procedure removes the severe near-boundary underestimation observed in Fig. 12(b) and substantially restricts the remaining diffusivity deviations. Some moderate errors remain near the screening transition because image sources with estimated contributions below 30% are intentionally neglected. As shown in Fig. 12(d), the synthetic energy curves generated using the full cuboid-domain solution were refitted using the single-boundary image-source formulation applied to all simulated cases, without contribution-based screening. The recovered diffusivities closely coincide with the prescribed values, demonstrating that explicitly retaining the single relevant boundary reflection is sufficient to reproduce the prescribed parameters embedded in the full cuboid-domain synthetic data for the present controlled configuration.

Because diffusivity and dissipation are estimated simultaneously from the same logarithmic energy evolution, assessing only the recovered diffusivity would provide an incomplete evaluation of the influence of boundary-model mismatch on parameter estimation. Although the dissipation coefficient does not explicitly appear in the image-source contribution ratio because the common dissipation term cancels between the direct-source and image-source energies, neglecting reflected energy introduces an additional time-dependent term into the logarithmic energy evolution. This omitted term may alter the fitted temporal decay and consequently bias not only the diffusivity but also the simultaneously estimated dissipation. Fig. 12(e) therefore presents the dissipation coefficients obtained directly from the infinite-medium fits used in Fig. 12(b), without applying the 30% threshold or any reflection correction. A comparison between Fig. 12(b) and (e) shows that the dissipation coefficients remain considerably closer to their prescribed values than the corresponding diffusivities. In particular, the pronounced distance-dependent underestimation, subsequent overestimation, and gradual convergence observed for diffusivity in Fig. 12(b) are not evident to the same extent in the dissipation results. This indicates that, under the investigated conditions, the model discrepancy caused by neglecting reflected energy is accommodated predominantly through changes in the fitted diffusivity, whereas the dissipation coefficient is comparatively less sensitive to the boundary contribution.

Fig. 12(f) summarizes the relative diffusivity errors exceeding 0.1% for the simulated parameter and boundary-distance combinations. Cases with errors at or below 0.1% were omitted from the violin visualization solely to improve the visibility of the non-negligible error distributions. The infinite-medium results exhibit a pronounced high-error tail, with the largest individual error approaching 19%. After applying the 30% threshold-guided scheme, this high-error tail is substantially suppressed, and the largest observed error is reduced to approximately 5%. Thus, the principal benefit of the screening procedure is not merely a change in the median error but a substantial reduction in the occurrence and magnitude of large boundary-induced errors. The remaining errors are not expected to vary monotonically with the estimated image-source contribution. As demonstrated by the sign-changing bias in Fig. 12(b), an infinite-medium estimate may temporarily cross the prescribed diffusivity and consequently exhibit a small absolute error even while the reflected contribution remains appreciable. Such isolated agreement represents incidental cancellation rather than model robustness.

The approximately 30% reference level is suggested by the combined contribution estimates and fitting comparisons for the predefined reflection configurations across the four members. In the controlled single-boundary numerical analysis, using this level to select between the infinite-medium and reflection-inclusive formulations reduced the largest observed relative diffusivity error from 19% to 5%. This result illustrates how contribution-based screening can reduce substantial parameter-estimation errors caused by omitting reflected energy under the investigated conditions. However, the remaining errors demonstrate that this reference level does not guarantee a prescribed parameter-recovery accuracy. Its suitability should therefore be assessed against the geometry, measurement configuration, and accuracy requirements of the intended application.

More broadly, the proposed approach provides a contribution-based assessment of candidate image sources using the relevant member geometry, sensor positions, expected diffusivity range, fitting-time interval, and boundary assumptions. Its extension to other members requires the adopted diffusion and image-source representations to remain applicable. Independent studies involving different materials, geometries, sensor arrangements, and boundary configurations are needed to evaluate the resulting reflection selections and establish suitable screening levels for those applications.

The noise-free responses and exactly specified sensor coordinates adopted in this section provide a controlled reference for examining the influence of reflected energy on parameter estimation. With the input transport properties and source-receiver distance fixed, varying the source-to-boundary distance changes the image-source contribution under a prescribed geometry. For each configuration, identical coordinates are used in response generation and fitting, excluding sensor-position mismatch as an additional source of error. These conditions allow the effect of retaining or omitting the reflected-energy term to be examined without measurement-noise effects and support interpretation of the 30% reference level under the specified single-boundary conditions. Its performance with noisy measurements or uncertain sensor coordinates requires further assessment.

5.2. Applicability and practical considerations of the proposed method

The proposed method selects the boundary reflections to be included in diffusion fitting according to the predicted energy contributions of the corresponding image sources relative to the real source. Applying this procedure to a different member requires recalculating the source-receiver and image-source-receiver distances from its geometry and sensor positions, and specifying an appropriate diffusivity range and fitting-time interval. The adopted diffusion and boundary assumptions must also remain applicable. The present experiments demonstrate agreement with the cuboid-domain reference only for the investigated geopolymer concrete configurations with embedded sensors and approximately planar free concrete-air boundaries under the adopted geometric approximation. Further independent studies covering other concrete materials, member geometries, or sensor configurations are needed to assess the applicability of the image-source selection procedure beyond the present structural system.

The governing contribution calculation does not explicitly contain the concrete mixture type; however, its experimental performance has so far been demonstrated only for the tested geopolymer-concrete structural system. At the same time, the absolute values of diffusivity and dissipation obtained in this study should be regarded as material-specific and cannot be directly transferred to ordinary Portland-cement concrete. In ordinary Portland-cement concrete, body-wave scattering in the several-hundred-kilohertz range is likely to be strongly influenced by the interfacial transition zone (ITZ) surrounding coarse aggregates [17,70], whereas in geopolymer concrete with a mechanically stronger ITZ [71,72], the dominant scattering source may shift toward the coarse aggregates themselves. As diffusivity reflects the effective scattering strength of the medium, these differences in *meso*-structure and dominant scattering phase provide a plausible explanation for why the absolute diffusivity and dissipation values obtained in the present geopolymer members should not be directly transferred to ordinary Portland-cement concrete.

Additionally, caution should be exercised when using elastic waves with extremely high frequencies, for which the wavelength is much shorter than the characteristic size of scatterers in concrete. Under such conditions, wave localization may occur [73], and the energy transport can no longer be described by the diffusion equation [74]. In addition, the proposed method is intended for body waves, which propagate three-dimensionally within the medium. For this reason, embedded sensors are preferred, and the distance from the sensor to the nearest boundary should be greater than the Rayleigh wavelength corresponding to the lowest frequency of interest [66]. For surface-bonded sensors, the experimental setup must be designed with particular care, because these sensors detect both surface and body waves, and decoupling their contributions during post-processing can be difficult. Finally, it is not necessary to

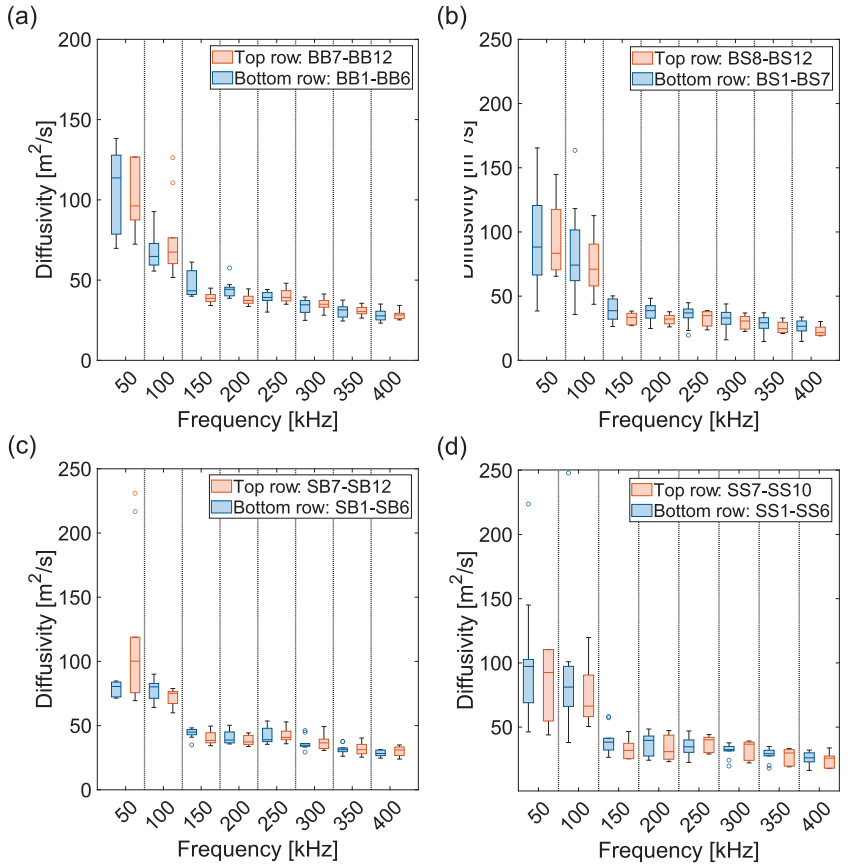


Fig. 13. Comparison of fitted diffusivity using Case VI from top-row and bottom-row sensor pairs in Beam I (a), Beam II (b), Beam III (c), and Beam IV (d).

include all image sources in the fitting model. Instead, only those reflections whose contributions to the direct energy remain sufficiently large at the maximum elapsed time need to be retained. In the present study, the reference lapse time for estimating reflection contributions is 800 μs. Based on the combined experimental comparisons, approximately 30% is suggested as an empirical reference level for reflection screening in similar configurations.

5.3. *Possible influence of the prefabricated-topping solid–solid interface*

The influence of solid–solid interfaces on elastic diffusivity remains difficult to quantify. Previous studies [41,75] have suggested that elastic diffusivity is related to the diffusivity of longitudinal and transverse waves, as well as to the energy equilibration ratio. The diffusivities of different wave modes are further influenced by wave velocity and the transport mean free path, which is inversely correlated with the total scattering cross-section [76]. In an energy-conserving system with constant wave velocities, the presence of solid–solid boundaries introduces additional scattering events, leading to a larger total scattering cross-section and a smaller transport mean free path. Consequently, both the diffusivities of longitudinal and transverse waves are expected to be smaller. Additionally, the energy equilibration ratio may also be affected by a solid–solid interface [77]. Therefore, the presence of such an interface may affect the fitted elastic diffusivity.

In this section, the possible influence of the solid–solid interface between the prefabricated beam and the cast-in-situ topping layer was examined by comparing the fitted diffusivities obtained from the top-row and bottom-row sensor pairs. The top-row sensors are located closer to this interface, whereas the bottom-row sensors are farther away. Therefore, if the interface produced a strong and systematic effect on the fitted diffusivity, a consistent difference between the two rows would be expected.

As shown in Fig. 13, row-to-row differences are observed in diffusivities, especially at low frequencies where the scatter of diffusivity is also larger. However, no consistent bias is found in which the top-row results are systematically higher or lower than the bottom-row results across the tested members and frequency range. The observed row-to-row differences should therefore be interpreted with caution. They may result from a combination of spatial variation within the heterogeneous concrete members and the possible influence of the prefabricated-topping interface. These two effects cannot be separated strictly using the present dataset. Spatial variation of concrete heterogeneity is expected to contribute mainly to random scatter among different sensor pairs, whereas a dominant interface effect would be expected to produce a more systematic trend associated with the distance between the sensors and

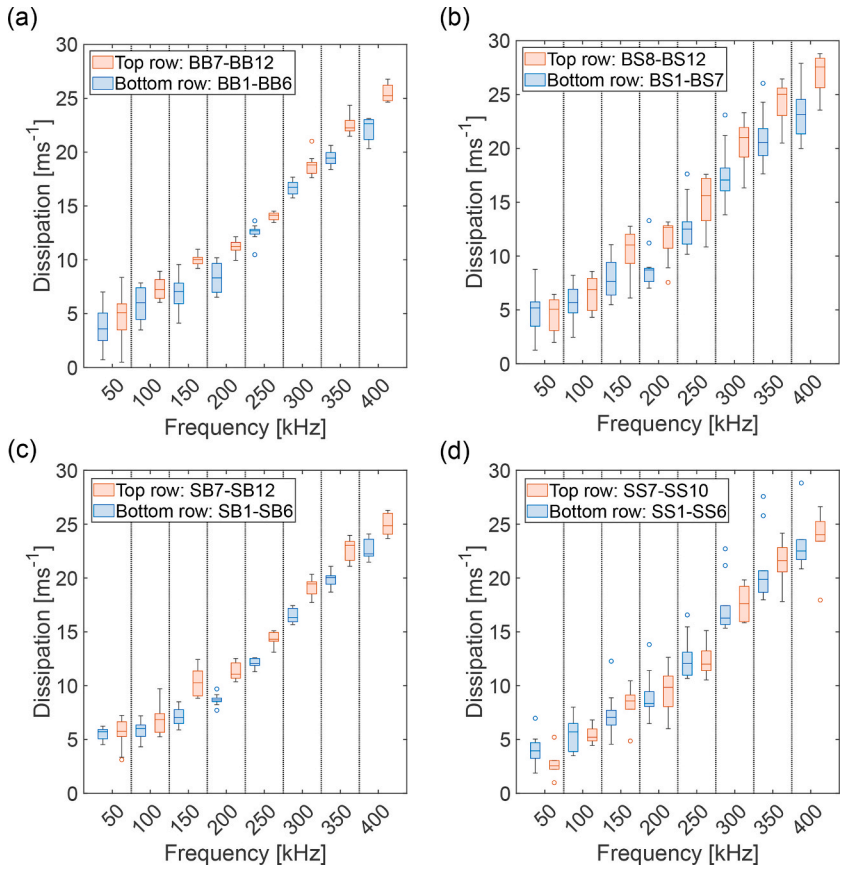


Fig. 14. Comparison of fitted dissipation using Case VI from top-row and bottom-row sensor pairs in Beam I (a), Beam II (b), Beam III (c), and Beam IV (d).

the interface. The absence of such a consistent trend suggests that the interface may contribute to the observed variability, but it does not appear to act as a dominant systematic factor in the fitted diffusivity.

Regarding dissipation, the top-row sensor pairs generally show higher fitted values than the bottom-row sensor pairs, especially at medium and high frequencies, as shown in Fig. 14. This indicates that the effective energy decay is faster in the region closer to the prefabricated-topping interface. Several mechanisms may contribute to this observation. First, the geopolymer concrete in the cast-in-situ topping layer may have higher intrinsic dissipation than that in the prefabricated prestressed beam, which could increase the apparent dissipation for sensor pairs located closer to the interface. Second, part of the elastic-wave energy may be transmitted or leaked across the prefabricated-topping interface, or redistributed through interface-related scattering and mode conversion, thereby increasing the effective energy loss observed in the prefabricated beam region. Similar interface-related leakage effects have been discussed by Trégourès and van Tiggelen [77]. Third, the bottom region of the prestressed beam may experience a higher compressive stress state, which could reduce dissipation if internal-friction-related mechanisms dominate the energy loss process [60]. However, these possible mechanisms cannot be separated quantitatively using the present dataset. Therefore, the comparison in Fig. 14 should be interpreted as evidence that the prefabricated-topping interface and the local structural condition may contribute to the spatial variability of fitted dissipation, rather than as a rigorous isolation of a single interface-induced effect.

More importantly, the main comparisons in this study concern the treatment of external concrete-air boundary reflections under the same measurements. The possible influence of the solid–solid interface is therefore shared by the different fitting cases and mainly affects the effective fitted properties. It does not invalidate the comparison between formulations that neglect or include external concrete-air boundary reflections. Consequently, the presence of the prefabricated-topping interface does not alter the main conclusion that external planar concrete-air boundary reflections need to be considered when estimating diffusive properties in the tested bounded members. It should be noted that the present comparison does not provide a strict quantitative isolation of the interface effect, because all members contain the same prefabricated-topping interface and no reference member without a topping layer was tested. A rigorous quantification of the influence of solid–solid interfaces would require a dedicated investigation of how such interfaces modify reflection, transmission, mode conversion, energy equilibration, and diffusive transport in heterogeneous concrete members. This issue therefore remains to be studied in future work.

5.4. *Range of validity and consistency check of the diffusion approximation*

Another important issue in applying the diffusion equation to concrete is its range of validity, as also discussed by Seher et al. [38]. The diffusion equation assumes that the wave field has entered the diffusive regime. It should be clarified that the Rayleigh regime, stochastic regime, and high-frequency limit discussed earlier describe scattering regimes determined by the relation between wavelength and heterogeneity size. They are therefore different from the diffusive regime, which is a later-time transport regime reached after sufficient multiple scattering and mode conversion. Multiple scattering in the Rayleigh or stochastic scattering regime can drive the wave field toward diffusion, but the occurrence of scattering alone does not automatically guarantee that the diffusion approximation is valid.

Ryzhik et al. [78] proposed an effective criterion for the validity of the diffusion approximation for elastic waves: the modal energies of longitudinal and transverse waves should have reached equilibration. Once this condition is reached, the P- and S-wave energy ratio becomes approximately stable. Mode conversion may still occur microscopically, but its net effect no longer needs to be explicitly resolved in a scalar diffusion formulation; instead, it is incorporated into the effective diffusivity governing the transport of the total elastic energy.

To examine whether this condition is reasonable for the present concrete members, a theoretical estimate of multiple scattering and mode conversion was performed using the framework developed in our previous work [79]. This framework estimates the scattering cross-sections and the corresponding diffusivity from *meso*-structural parameters of concrete. The expressions used for the scattering cross-sections and diffusivity are given in Appendix A, and the key parameters adopted in the calculation are listed in Table 12. Two checks were performed. First, the magnitude and frequency dependence of the fitted diffusivity were compared with the scattering-based theoretical prediction. Second, the energy equilibration time was estimated using the same scattering framework.

Fig. 15 compares the theoretical diffusivity with the fitted diffusivities obtained from Cases I, III, and VI. These three cases include the results from all four members. As shown in this figure, the theoretical prediction and the experimental fitting results show comparable magnitudes and the same decreasing trend with increasing frequency. Please note that the comparison is used only as a

Table 12
Key parameters used for the scattering-based theoretical calculations.

Physical quantity	Value [unit]
Property-contrast between coarse aggregates and geopolymer matrix A_{ij}	1* [-]
Longitudinal wave velocity v_P	4544 [m/s]
Transverse wave velocity v_S	2772 [m/s]
Volume fraction of coarse aggregates ϕ_s	25.7% [-]
Characteristic correlation length H	23.07 [mm]

*The value $A_{ij} = 1$ is adopted as an effective contrast factor for the theoretical consistency check and is not fitted from the present diffusion measurements. A detailed discussion of the selection of this value is provided in our previous paper [79].

physical plausibility check, not as an independent ground truth for the fitted diffusivity.

Assuming that the total elastic-wave energy E is conserved and can be expressed as the sum of the longitudinal-wave energy (E_P) and transverse-wave energy (E_S), the mode-conversion process can be described as [80]:

$$\frac{dE_P}{dt} = \frac{v_S^3}{2v_P^2}\Sigma_{PS}E - \frac{2v_P^3 + v_S^3}{2v_P^2}\Sigma_{PS}E_P \quad . \tag{7a}$$

For an initially longitudinal-wave source with normalized total energy, the analytical solution of Eq. (7a) is given by:

$$E_P = \frac{v_S^3}{2v_P^3 + v_S^3} + \frac{2v_P^3}{2v_P^3 + v_S^3} e^{-\frac{t}{\frac{2v_P^2}{2v_P^3+v_S^3}\frac{1}{\Sigma_{PS}}}} \quad . \tag{7b}$$

Using the total scattering cross-sections calculated from the parameters in Table 12, the evolution of the energy ratio E_S/E_P at 50 kHz is shown in Fig. 16. The result indicates that the ratio approaches an approximately stable value after about 80 μs. Because 50 kHz gives the largest predicted diffusivity among the analysed frequency bands, it corresponds to relatively weak scattering and therefore provides a conservative estimate of the equilibration time. The result suggests that global P/S energy equilibration is likely to have been reached before or within the time windows used for diffusion fitting. Therefore, although this simplified calculation neglects dissipation and should not be regarded as a complete proof of the diffusion approximation, it supports the use of the diffusion equation for the later coda portion analysed in this study. A more detailed investigation of energy equilibration in concrete will be addressed in future work.

5.5. Sensitivity to fitting-window selection

To further examine the rationale for the time-window configuration used in Section 4.1.1, a sensitivity analysis of fitting-window selection was performed. Four time-window configurations were considered, as summarized in Table 13. Configuration 1 corresponds to the baseline configuration used in the main analysis. Configurations 2 and 3 were designed to examine the influence of window length and shift before 800 μs, whereas Configuration 4 was designed to examine the influence of including later energy.

Fig. 17 compares the fitted logarithmic energy curves and the corresponding diffusivity and dissipation obtained using the four time-window configurations for Case III. The results show that the fitted parameters are affected by the window configuration, as expected. However, the main frequency-dependent trends remain unchanged.

Configuration 2, which uses 100 μs windows throughout the analysed coda before 800 μs, produces larger scatter at low frequencies and generally lower fitted diffusivity in several frequency bands. This is attributed to the reduced temporal resolution around the rising part and the energy maximum. Since diffusivity is strongly controlled by the early-time spreading rate and the position and shape of the energy maximum, overly long early windows can broaden the apparent peak region and weaken the constraint on diffusivity. This effect is particularly relevant at low frequencies, where the envelope evolves faster and boundary-reflected energy is more influential.

Configuration 3 gives results close to Configuration 1. This is reasonable because both configurations use short windows in the early coda, where the main information controlling diffusivity is contained. The use of short windows throughout the later coda retains more local fluctuations and residual coherent variations, which explains the larger low-frequency scatter. However, it does not substantially change the overall decay trend. Therefore, the fitted diffusivity and dissipation remain close to those obtained from the baseline Configuration 1.

Configuration 4 leads to more noticeable differences, especially in the fitted dissipation at high frequencies. In this setup, later coda

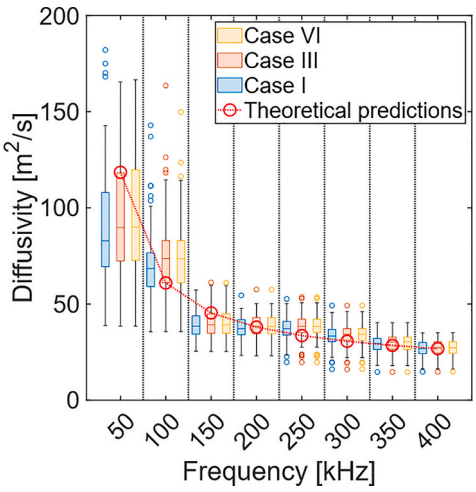


Fig. 15. Comparison between scattering-based theoretical predictions and experimentally fitted diffusivities from Cases I, III, and VI.

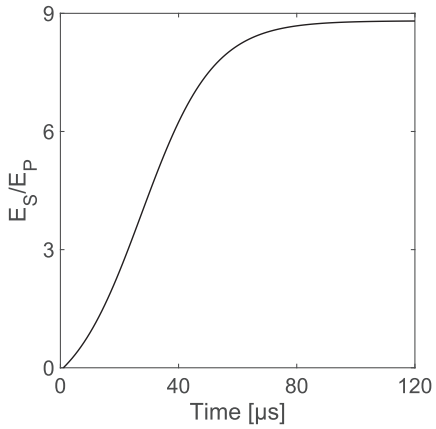


Fig. 16. Predicted evolution of the transverse-to-longitudinal energy ratio E_S/E_P for an initially longitudinal-wave source at 50 kHz.

Table 13
Time-window configurations used for the fitting-window sensitivity analysis.

Time window configuration	Purpose of comparison	Early window setting	Late window setting	Number of windows
1	Baseline setup used in the main analysis	40 μs window with 20 μs shift from 25 μs to 225 μs	100 μs window with 50 μs shift from 225 μs to 725 μs	22
2	Test the influence of using longer windows before 800 μs	100 μs window with 50 μs shift before 800 μs from 25 μs to 725 μs		15
3	Test the influence of using shorter windows before 800 μs	40 μs window with 20 μs shift before 800 μs from 25 μs to 765 μs		38
4	Test the influence of including later energy	40 μs window with 20 μs shift from 25 μs to 325 μs	100 μs window with 50 μs shift from 325 μs to 1075 μs	32

energy beyond the baseline fitting range is included. At high frequencies, the energy after approximately 800 μs approaches the noise floor, and including this late low-energy portion reduces the apparent slope of the logarithmic energy decay. This directly lowers the fitted dissipation and can also affect the fitted diffusivity through parameter coupling in the nonlinear fitting. This observation supports the use of the original fitting range, which avoids excessive influence from the late noise-dominated coda while retaining sufficient information for diffusion fitting.

Fig. 18 compares the fitted diffusivity and dissipation obtained from Cases I, III, and VI in Beam I under the alternative time-window configurations. The results show that the absolute fitted values are affected by the window configuration. This effect is particularly visible at low frequencies for diffusivity and at high frequencies for dissipation, where the fitted parameters are more sensitive to the representation of the early energy build-up and the late-time decay, respectively. Nevertheless, the relative behaviour among the three fitting cases remains consistent for all tested window configurations. In Configurations 2, 3, and 4, the results obtained from Case III are consistently closer to those from Case VI than those obtained from Case I. Although changing the fitting windows can alter the numerical values of the fitted parameters, it does not remove the systematic discrepancy caused by neglecting reflected energy.

This behaviour can be understood from the construction of the three formulations. Case I omits reflected-energy contributions entirely, whereas Case III retains the dominant image sources that are also represented in the full cuboid-domain formulation. The retained image sources are not additional free fitting parameters; their locations and source-receiver distances are determined by the specimen geometry and boundary locations. Therefore, the closer agreement between Case III and Case VI reflects the inclusion of physically determined dominant reflected-energy terms. For the fitting-window configurations examined, Case III generally remains closer to Case VI than Case I, although the absolute fitted diffusivity and dissipation vary with window selection. These results support the persistence of the observed benchmark agreement under the tested window configurations.

5.6. Potential relevance to concrete monitoring and future work

The diffusive properties estimated in the present study are of practical interest for concrete monitoring. According to previous research, potential applications of diffusivity and dissipation in concrete include characterizing the properties of heterogeneity in concrete [21,35,70], evaluating cracking damage in concrete [16,22–24,27–29,33,36,38,40], assessing the self-healing process of concrete [37,39], investigating water depercolation in cement paste [26], evaluating thermal damage in concrete [17], and localizing damage in concrete structures [18,81,82].

The same full-scale members and embedded sensor network have recently been investigated in a separately reported loading

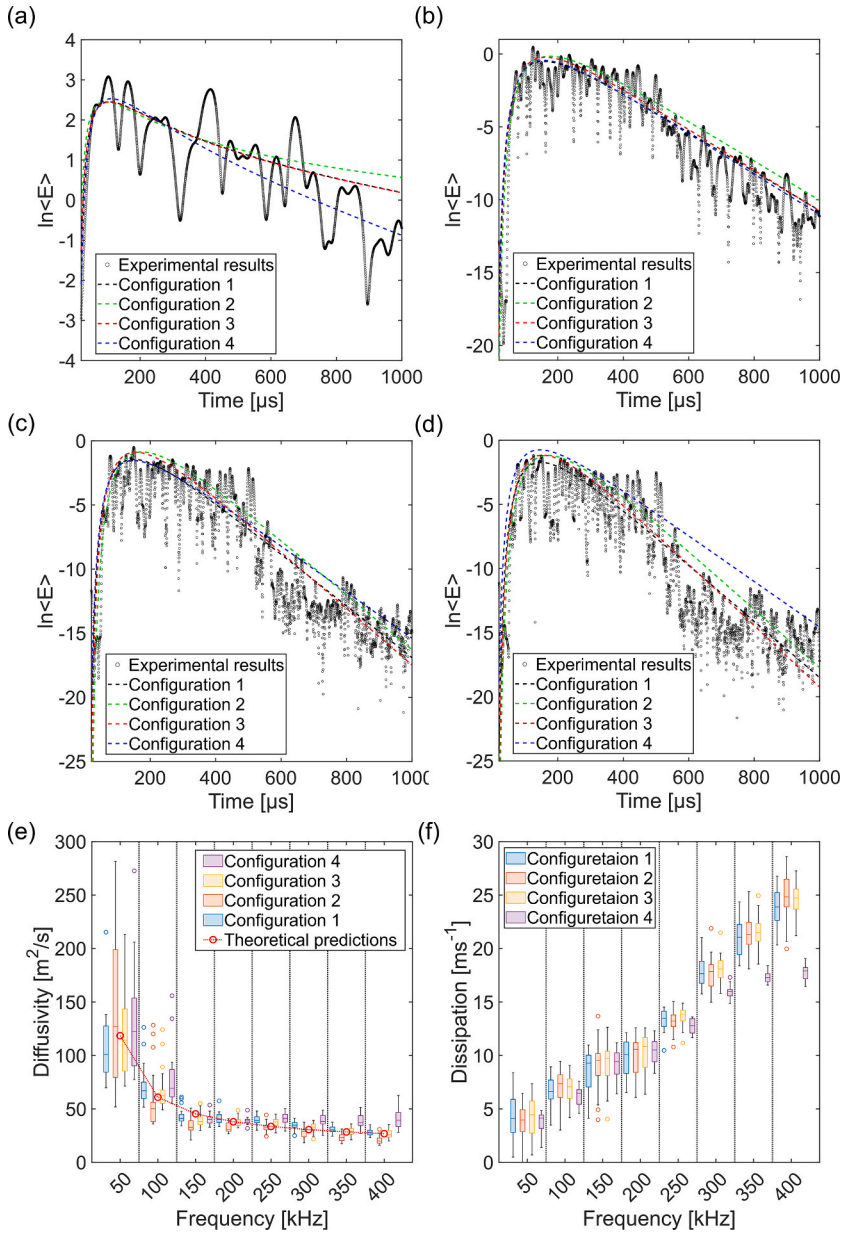


Fig. 17. Sensitivity of Case III fitting results to different time-window configurations in Beam I. Panels (a)-(d) show representative logarithmic energy fittings at 50, 250, 300, and 400 kHz, respectively. Panels (e) and (f) compare the fitted diffusivity and dissipation obtained from all sensor pairs. Configuration 1 is the baseline configuration used in the main analysis, whereas Configurations 2–4 are alternative configurations used for the sensitivity analysis. In panels (a)-(d), the black scatter points show the unwindowed sampled energy values for visual comparison, whereas the fitted curves are obtained from the window-averaged energies used in the fitting procedure.

campaign, in which ultrasonic measurements were correlated with DIC-observed crack development and changes in the global structural response [83]. However, the present study evaluates parameter estimation through comparisons with the full cuboid-domain diffusion benchmark and examines the computational cost of fitting. Agreement with this benchmark does not directly establish improved performance in damage detection or localization. No downstream damage-detection or localization task is demonstrated, and the effects of the proposed parameter-estimation procedure on damage sensitivity, localization accuracy, and structural health monitoring (SHM) decision making remain unquantified. Its relevance to SHM is therefore limited to its potential use as a parameter-estimation step in a broader monitoring procedure. Evaluating the estimated properties in such a procedure, with independently characterized damage states, remains a subject for future investigation.

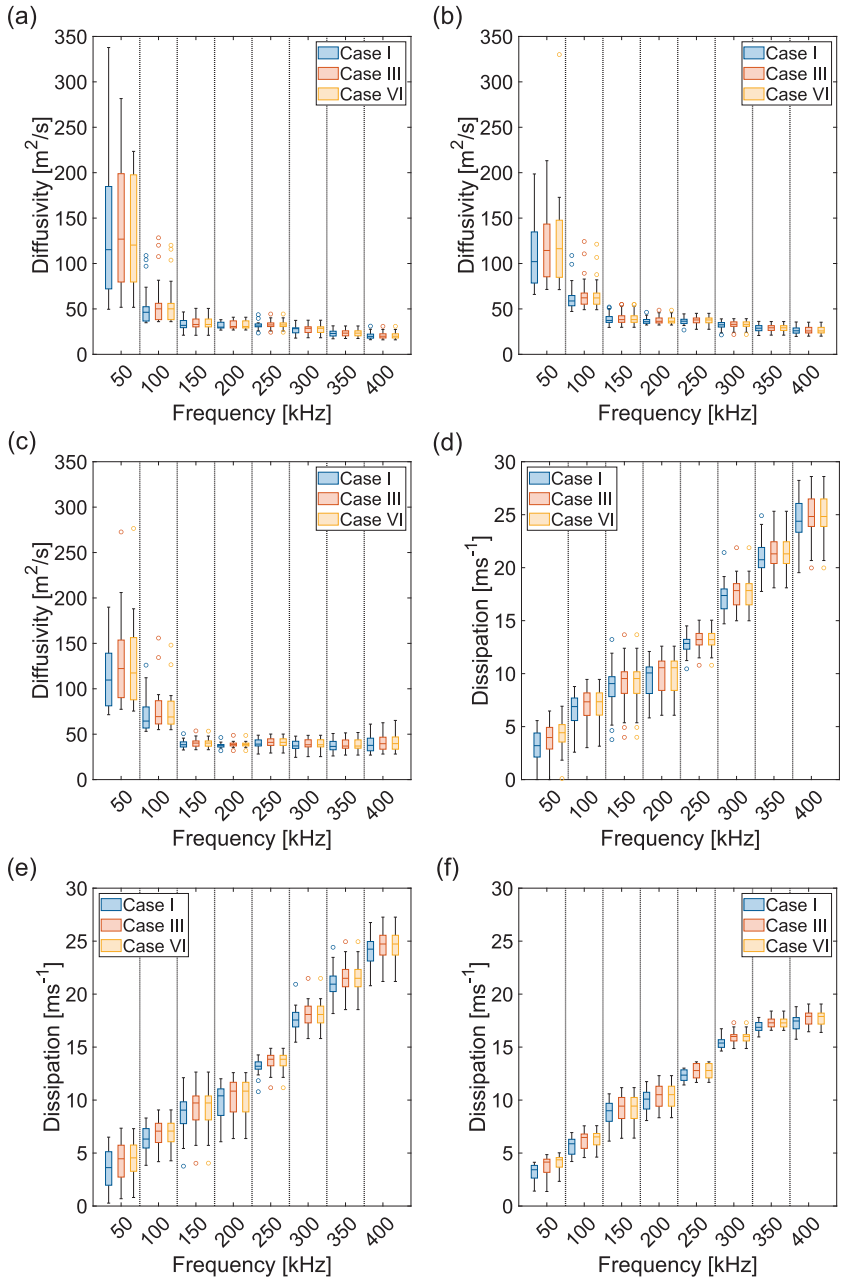


Fig. 18. Comparison of Cases I, III, and VI under alternative time-window configurations in Beam I. Panels (a)-(c) show the fitted diffusivity obtained using Configurations 2, 3, and 4, respectively. Panels (d)-(f) show the corresponding fitted dissipation.

6. Conclusions

This study shows that boundary reflections play a non-negligible role in the estimation of diffusivity and dissipation of diffuse body waves in bounded concrete members with approximately planar free concrete-air boundaries, and that their influence can be captured with high agreement with the full cuboid-domain diffusion benchmark. Based on the experimental and comparative analyses, the following conclusions can be drawn:

1. In the investigated experimental configurations, neglecting reflected energy generally yielded lower fitted diffusivity and dissipation than those obtained with Case VI, with the largest discrepancies occurring at low frequencies. This result quantifies the fitting bias caused by neglecting reflected energy, rather than being presented as a new physical mechanism.

2. The influence of boundary reflections is strongly frequency dependent. In both the pair-level and beam-level analyses, the effect of reflected energy is substantial at 50 and 100 kHz and becomes progressively less important as frequency increases. At the same time, the fitted properties exhibit consistent frequency dependence across members: diffusivity decreases with increasing frequency, whereas dissipation increases with increasing frequency. The decreasing diffusivity is consistent with the scattering-based theoretical prediction and previous diffuse-wave studies, and is used here as a physical consistency check rather than as a new frequency-dependent trend. The increasing dissipation is reported as an experimental trend consistent with previous observations, without claiming a new mechanistic interpretation.
3. For the evaluated Case III configurations, the mean relative differences in diffusivity and dissipation from the full cuboid-domain benchmark remained below 2%. Including additional reflection terms provided only marginal further improvement. Considering these fitting comparisons together with the estimated reflection contributions, approximately 30% is suggested as an empirical reference level for reflection screening under conditions comparable to those investigated here. Its performance as a fixed numerical cutoff requires independent validation.
4. Retaining the dominant image-source contributions provides close agreement with the cuboid-domain benchmark at a lower fitting cost. For the 160-fit workload in Beam I, the mean fitting times for Cases I-V ranged from 1.98 to 2.23 s, compared with 6.24 s for the vectorized Case VI implementation, corresponding to a reduction of approximately 66%. This computational advantage is specific to the workload, implementations, and truncation settings examined. Case VI remains a bounded-domain computational benchmark rather than an independently measured physical ground truth.
5. Although the overall frequency dependence remains consistent across members, diffusivity shows noticeable variation from beam to beam even within the same structural system, indicating that it is spatially sensitive to local heterogeneity, sensor location, and wave-propagation path. This suggests that diffusivity should not be interpreted as a unique constant at the member scale, but rather as a parameter that reflects the local characteristics of diffusive wave transport in concrete. The absolute values of diffusivity and dissipation obtained from the present geopolymer concrete members should not be directly transferred to other concrete materials. However, the contribution-based image-source selection procedure can be recalibrated for other bounded concrete members using their own geometry, sensor layout, expected diffusivity range, fitting time window, and boundary conditions.

CRediT authorship contribution statement

Hao Cheng: Writing – original draft, Visualization, Validation, Software, Methodology, Investigation, Formal analysis, Data curation. **Katrin Löer:** Writing – review & editing, Visualization, Supervision. **Max A.N. Hendriks:** Writing – review & editing, Supervision, Resources, Project administration. **Yuguang Yang:** Writing – review & editing, Visualization, Supervision, Resources, Project administration, Methodology, Funding acquisition, Conceptualization.

Declaration of competing interest

The authors declare that they have no known competing financial interests or personal relationships that could have appeared to influence the work reported in this paper.

Appendix A. Total scattering cross-sections in concrete and their relationship to diffusivity

In this paper, we adopt the expressions for total scattering cross-sections in concrete reported in our previous work [79]:

$$\Sigma_{\mathrm{PP}} = \frac{A_{ij}\phi_{\mathrm{s}}(1-\phi_{\mathrm{s}})H^3\omega^4}{v_{\mathrm{P}}^4}\int_{-1}^{+1}\frac{\frac{\left(v_{\mathrm{P}}^2-2v_{\mathrm{S}}^2\right)^2}{v_{\mathrm{P}}^4}+\frac{2\left(v_{\mathrm{P}}^2-2v_{\mathrm{S}}^2\right)}{v_{\mathrm{P}}^2}\chi+\left[\frac{4v_{\mathrm{S}}^2\left(v_{\mathrm{P}}^2-2v_{\mathrm{S}}^2\right)}{v_{\mathrm{P}}^4}+1\right]\chi^2+\frac{4v_{\mathrm{S}}^2}{v_{\mathrm{P}}^2}\chi^3+\frac{4v_{\mathrm{S}}^4}{v_{\mathrm{P}}^4}\chi^4}{\left(1+2x_{\mathrm{P}}^2-2x_{\mathrm{P}}^2\chi\right)^2}\mathrm{d}\chi\ , \tag{A1a}$$

$$\Sigma_{\mathrm{SS}} = \frac{A_{ij}\phi_{\mathrm{s}}(1-\phi_{\mathrm{s}})H^3\omega^4}{v_{\mathrm{S}}^4}\int_{-1}^{+1}\frac{1-\chi^2+2\chi^3+2\chi^4}{\left(1+2x_{\mathrm{S}}^2-2x_{\mathrm{S}}^2\chi\right)^2}\mathrm{d}\chi\ , \tag{A1b}$$

$$\Sigma_{\mathrm{PS}} = \frac{A_{ij}\phi_{\mathrm{s}}(1-\phi_{\mathrm{s}})H^3\omega^4}{v_{\mathrm{P}}v_{\mathrm{S}}^3}\int_{-1}^{+1}\frac{(1-\chi^2)\left(1+\frac{4v_{\mathrm{S}}}{v_{\mathrm{P}}}\chi+\frac{4v_{\mathrm{S}}^2}{v_{\mathrm{P}}^2}\chi^2\right)}{\left(1+x_{\mathrm{P}}^2+x_{\mathrm{S}}^2-2x_{\mathrm{P}}x_{\mathrm{S}}\chi\right)^2}\mathrm{d}\chi\ , \tag{A1c}$$

$$\Sigma_{\mathrm{SP}} = \frac{A_{ij}\phi_{\mathrm{s}}(1-\phi_{\mathrm{s}})H^3\omega^4}{2v_{\mathrm{P}}^3v_{\mathrm{S}}}\int_{-1}^{+1}\frac{(1-\chi^2)\left(1+\frac{4v_{\mathrm{S}}}{v_{\mathrm{P}}}\chi+\frac{4v_{\mathrm{S}}^2}{v_{\mathrm{P}}^2}\chi^2\right)}{\left(1+x_{\mathrm{P}}^2+x_{\mathrm{S}}^2-2x_{\mathrm{P}}x_{\mathrm{S}}\chi\right)^2}\mathrm{d}\chi\ , \tag{A1d}$$

where A_{ij} is defined as the contrast of the properties for the coarse aggregates and geopolymer matrix shown in this paper [79], ω represents the angular frequency, ϕ_{s} indicates the volume fraction of coarse aggregates, v_{P} and v_{S} denote longitudinal wave and transverse wave velocities in the heterogeneous medium (average among different phases). The parameter χ is defined as the cosine of the scattering angle, $\cos\theta_{\mathrm{s}}$, between the incident wave vector $\mathbf{k}_{\mathrm{K}}=(\omega/v_{\mathrm{K}})\mathbf{p}$ and scattered wave vector $\mathbf{k}_{\mathrm{L}}=(\omega/v_{\mathrm{L}})\mathbf{p}'$, where superscripts K

(K∈{P,S}) and L (L∈{P,S}) represent the modes of incident and scattered waves, respectively. Parameters x_K and x_L are dimensionless frequencies defined as $x_K = \omega H/v_K$ and $x_L = \omega H/v_L$, respectively. The parameter H denotes the characteristic correlation length, which can be estimated through:

$$H = \frac{4r_s}{3\phi_s} \quad , \tag{A2}$$

where r_s indicates the characteristic radius of coarse aggregates and can be calculated through:

$$r_s = \left(\sum_{i=1}^{g} \frac{n_i}{r_i^3} \right)^{-\frac{1}{3}} \quad , \tag{A3}$$

where n_i denotes the volume ratio within the grading interval i, and r_i is the maximum radius within this grading interval. The subscript g denotes the total number of grading intervals.

When deriving diffusivity from total scattering cross-sections, weighted total scattering cross-sections [75], which account for the propagation preference and include a weighting factor based on the cosine of the scattering angle in the integral [48], are required and are defined as [79]:

$$\Sigma'_{PP} = \frac{A_{ij}\phi_s(1-\phi_s)H^3\omega^4}{v_P^4} \int_{-1}^{+1} \chi d\chi \frac{\frac{\left(v_P^2-2v_S^2\right)^2}{v_P^4} + \frac{2\left(v_P^2-2v_S^2\right)}{v_P^2}\chi + \left[\frac{4v_S^2\left(v_P^2-2v_S^2\right)}{v_P^4}+1\right]\chi^2 + \frac{4v_S^2}{v_P^2}\chi^3 + \frac{4v_S^4}{v_P^4}\chi^4}{\left(1+2x_P^2-2x_P^2\chi\right)^2} \quad , \tag{A4a}$$

$$\Sigma'_{SS} = \frac{A_{ij}\phi_s(1-\phi_s)H^3\omega^4}{v_S^4} \int_{-1}^{+1} \chi d\chi \frac{1-\chi^2+2\chi^3+2\chi^4}{\left(1+2x_S^2-2x_S^2\chi\right)^2} \quad , \tag{A4b}$$

$$\Sigma'_{PS} = \frac{A_{ij}\phi_s(1-\phi_s)H^3\omega^4}{v_P v_S^3} \int_{-1}^{+1} \chi d\chi \frac{(1-\chi^2)\left(1+\frac{4v_S}{v_P}\chi+\frac{4v_S^2}{v_P^2}\chi^2\right)}{\left(1+x_P^2+x_S^2-2x_P x_S\chi\right)^2} \quad , \tag{A4c}$$

$$\Sigma'_{SP} = \frac{A_{ij}\phi_s(1-\phi_s)H^3\omega^4}{2v_P^3 v_S} \int_{-1}^{+1} \chi d\chi \frac{(1-\chi^2)\left(1+\frac{4v_S}{v_P}\chi+\frac{4v_S^2}{v_P^2}\chi^2\right)}{\left(1+x_P^2+x_S^2-2x_P x_S\chi\right)^2} \quad . \tag{A4d}$$

After acquiring both weighted total scattering cross-sections and total scattering cross-sections, the transport mean free path can be obtained through [41,75,76]:

$$l_P^* = \frac{\Sigma_{SS}+\Sigma_{SP}-\Sigma'_{SS}+\Sigma'_{PS}}{\left(\Sigma_{PP}+\Sigma_{PS}-\Sigma'_{PP}\right)\left(\Sigma_{SS}+\Sigma_{SP}-\Sigma'_{SS}\right)-\Sigma'_{PS}\Sigma'_{SP}} \tag{A5a}$$

$$l_S^* = \frac{\Sigma_{PP}+\Sigma_{PS}-\Sigma'_{PP}+\Sigma'_{SP}}{\left(\Sigma_{PP}+\Sigma_{PS}-\Sigma'_{PP}\right)\left(\Sigma_{SS}+\Sigma_{SP}-\Sigma'_{SS}\right)-\Sigma'_{PS}\Sigma'_{SP}} \tag{A5b}$$

and the diffusivity is given by [41,75,76,78]:

$$D = \frac{v_S^3\left(\frac{1}{3}v_P l_P^*\right)+2v_P^3\left(\frac{1}{3}v_S l_S^*\right)}{2v_P^3+v_S^3} \tag{A6}$$

Data availability

Data will be made available on request.

References

[1] S.K.U. Rehman, Z. Ibrahim, S.A. Memon, M. Jameel, Nondestructive test methods for concrete bridges: a review, Constr. Build. Mater. 107 (2016) 58–86.
[2] V.G.M. Annamdas, S. Bhalla, C.K. Soh, Applications of structural health monitoring technology in Asia, Struct. Health Monit. 16 (3) (2017) 324–346.
[3] P. Rizzo, A. Enshaeian, Bridge health monitoring in the United States: a review, Struct. Monit. Maint. Int. J. 8 (1) (2021) 1–50.
[4] N.K. Mutlib, S. Bin Baharom, A. El-Shafie, M.Z. Nuawi, Ultrasonic health monitoring in structural engineering: buildings and bridges, Struct. Control Health Monit. 23 (3) (2016) 409–422.

[5] G. Karaiskos, A. Deraemaeker, D.G. Aggelis, D. Van Hemelrijck, Monitoring of concrete structures using the ultrasonic pulse velocity method, Smart Mater. Struct. 24 (11) (2015) 18.
[6] T. Planès, E. Larose, A review of ultrasonic Coda Wave Interferometry in concrete, Cem. Concr. Res. 53 (2013) 248–255.
[7] E. Niederleithinger, X. Wang, M. Herbrand, M. Muller, Processing ultrasonic data by coda wave interferometry to monitor load tests of concrete beams, Sensors (Basel) 18 (6) (2018) 13.
[8] C. Dumoulin, A. Deraemaeker, All-season monitoring of concrete repair in an urban tunnel in Brussels using embedded ultrasonic transducers with emphasis on robustness to environmental variations, J. Civ. Struct. Health Monit. 11 (4) (2021) 879–895.
[9] B.B. Zhong, J.Y. Zhu, G. Morcous, Measuring acoustoelastic coefficients for stress evaluation in concrete, Constr. Build. Mater. 309 (2021) 125127.
[10] A. Derode, A. Tourin, M. Fink, Random multiple scattering of ultrasound. I. Coherent and ballistic waves, Phys. Rev. E Stat. Nonlin. Soft Matter Phys. 64 (3 Pt 2) (2001) 036605.
[11] H. Cheng, C. Weemstra, M.A.N. Hendriks, Y. Yang, Comparing the stretching technique and the wavelet cross-spectrum technique for measuring stress-induced wave-velocity changes in concrete, Autom. Constr. 158 (2024) 105221.
[12] E. Larose, S. Hall, Monitoring stress related velocity variation in concrete with a 2×10^{-5} relative resolution using diffuse ultrasound, J. Acoust. Soc. Am. 125 (4) (2009) 1853–1856.
[13] R. Snieder, A. Gret, H. Douma, J. Scales, Coda wave interferometry for estimating nonlinear behavior in seismic velocity, Science 295 (5563) (2002) 2253–2255.
[14] Y. Zhang, O. Abraham, V. Tournat, A. Le Duff, B. Lascoup, A. Loukili, F. Grondin, O. Durand, Validation of a thermal bias control technique for Coda Wave Interferometry (CWI), Ultrasonics 53 (3) (2013) 658–664.
[15] L. Wang, S. Yi, Y. Yu, C. Gao, B. Samali, Automated ultrasonic-based diagnosis of concrete compressive damage amidst temperature variations utilizing deep learning, Mech. Syst. Signal Proc. 221 (2024) 111719.
[16] E. Ahn, M. Shin, J.S. Popovics, Air-coupled ultrasonic diffuse-wave techniques to evaluate distributed cracking damage in concrete, Ultrasonics 125 (2022) 106800.
[17] M. Ramaniraka, S. Rakotonarivo, C. Payan, V. Garnier, Effect of Interfacial transition Zone on diffuse ultrasound in thermally damaged concrete, Cem. Concr. Res. 152 (2022) 106680.
[18] Y.X. Zhang, E. Larose, L. Moreau, G. d'Ozouville, Three-dimensional in-situ imaging of cracks in concrete using diffuse ultrasound, Struct. Health Monit. 17 (2) (2018) 279–284.
[19] H.Y. Zhan, H.W. Jiang, R.N.A. Jiang, Three-dimensional images generated from diffuse ultrasound wave: detections of multiple cracks in concrete structures, Struct. Health Monit. 19 (1) (2020) 12–25.
[20] V. Rossetto, L. Margerin, T. Planès, É. Larose, Locating a weak change using diffuse waves: theoretical approach and inversion procedure, J. Appl. Phys. 109 (3) (2011) 034903.
[21] F. Schubert, B. Koehler, Numerical time-domain simulation of diffusive ultrasound in concrete, Ultrasonics 42 (1–9) (2004) 781–786.
[22] A. Quiviger, C. Payan, J.F. Chaix, V. Garnier, J. Salin, Effect of the presence and size of a real macro-crack on diffuse ultrasound in concrete, NDT E Int. 45 (1) (2012) 128–132.
[23] C. Payan, A. Quiviger, V. Garnier, J.F. Chaix, J. Salin, Applying diffuse ultrasound under dynamic loading to improve closed crack characterization in concrete, J. Acoust. Soc. Am. 134 (2) (2013) EL211–EL216.
[24] A. Quiviger, A. Girard, C. Payan, J.F. Chaix, V. Garnier, J. Salin, Influence of the depth and morphology of real cracks on diffuse ultrasound in concrete: a simulation study, NDT E Int. 60 (2013) 11–16.
[25] P. Shokouhi, A. Lorenz, Ultrasonic investigation of damage progression in concrete, AIP Conf. Proc., Am. Inst. Phys. (2014) 917–924.
[26] H.J. Yim, Y.K. An, J.H. Kim, Water depercolation of setting cement paste evaluated by diffuse ultrasound, Cem. Concr. Compos. 71 (2016) 10–19.
[27] E. Ahn, M. Shin, J.S. Popovics, R.L. Weaver, Effectiveness of diffuse ultrasound for evaluation of micro-cracking damage in concrete, Cem. Concr. Res. 124 (2019) 105862.
[28] H.W. Jiang, H.Y. Zhan, J.Q. Zhang, R.N. Jiang, Diffusion coefficient estimation and its application in interior change evaluation of full-size reinforced concrete structures, J. Mater. Civ. Eng. 31 (3) (2019) 04018398.
[29] I.V. Tinoco, R.C.A. Pinto, Evaluation of stiffness loss of reinforced concrete beams using the diffuse ultrasound method, Ultrasonics 117 (2021) 106540.
[30] S. Basu, S. Sasmal, Ultrasonic wave diffusion-based investigations on microstructural development in multi-scale cementitious materials, Constr. Build. Mater. 442 (2024) 137626.
[31] E. Ahn, H. Song, M. Shin, J.S. Popovics, Influence of moisture on the diffusion of ultrasound in concrete, Ultrasonics 147 (2025) 107529.
[32] Z. Yang, C. He, Q. Kong, C. Yuan, Monitoring the microcrack evolution in FRP-wrapped concrete using diffuse ultrasound, J. Build. Eng. (2025) 113009.
[33] F. Deroo, J.Y. Kim, J. Qu, K. Sabra, L.J. Jacobs, Detection of damage in concrete using diffuse ultrasound, J. Acoust. Soc. Am. 127 (6) (2010) 3315–3318.
[34] P. Anugonda, J.S. Wiehn, J.A. Turner, Diffusion of ultrasound in concrete, Ultrasonics 39 (6) (2001) 429–435.
[35] J. Becker, L.J. Jacobs, J.M. Qu, Characterization of cement-based materials using diffuse ultrasound, J. Eng. Mech. 129 (12) (2003) 1478–1484.
[36] S.K. Ramamoorthy, Y. Kane, J.A. Turner, Ultrasound diffusion for crack depth determination in concrete, J. Acoust. Soc. Am. 115 (2) (2004) 523–529.
[37] C.W. In, R.B. Holland, J.Y. Kim, K.E. Kurtis, L.F. Kahn, L.J. Jacobs, Monitoring and evaluation of self-healing in concrete using diffuse ultrasound, NDT E Int. 57 (2013) 36–44.
[38] M. Seher, C.W. In, J.Y. Kim, K.E. Kurtis, L.J. Jacobs, Numerical and experimental study of crack depth measurement in concrete using diffuse ultrasound, J. Nondestruct. Eval. 32 (1) (2013) 81–92.
[39] B. Hilloulin, J.B. Legland, E. Lys, O. Abraham, A. Loukili, F. Grondin, O. Durand, V. Tournat, Monitoring of autogenous crack healing in cementitious materials by the nonlinear modulation of ultrasonic coda waves, 3D microscopy and X-ray microtomography, Constr. Build. Mater. 123 (2016) 143–152.
[40] C.W. In, K. Arne, J.Y. Kim, K.E. Kurtis, L.J. Jacobs, Estimation of crack depth in concrete using diffuse ultrasound: validation in cracked concrete beams, J. Nondestruct. Eval. 36 (1) (2017) 1–9.
[41] R.L. Weaver, W. Sachse, Diffusion of ultrasound in a glass bead slurry, J. Acoust. Soc. Am. 97 (4) (1995) 2094–2102.
[42] P.M. Morse, H. Feshbach, Methods of theoretical physics, Am. J. Phys 22 (6) (1954) 410–413.
[43] J.H. Rindel, The use of computer modeling in room acoustics, J. Vibroeng. 3 (4) (2000) 219–224.
[44] E.P. Papadakis, Ultrasonic attenuation caused by scattering in polycrystalline metals, J. Acoust. Soc. Am. 37 (4) (1965) 711–717.
[45] F.E. Stanke, G.S. Kino, A unified theory for elastic wave propagation in polycrystalline materials, J. Acoust. Soc. Am. 75 (3) (1984) 665–681.
[46] L. Margerin, M. Campillo, B. Van Tiggelen, Monte Carlo simulation of multiple scattering of elastic waves, J. Geophys. Res.-Solid Earth 105 (B4) (2000) 7873–7892.
[47] R.G. Newton, Scattering Theory of Waves and Particles, Springer Science & Business Media, 2013.
[48] R.L. Weaver, Diffusivity of ultrasound in polycrystals, J. Mech. Phys. Solids 38 (1) (1990) 55–86.
[49] P.W. Anderson, The question of classical localization a theory of white paint? Philos. Mag. B 52 (3) (1985) 505–509.
[50] R.L. Weaver, Anderson localization of ultrasound, Wave Motion 12 (2) (1990) 129–142.
[51] S. Chandrasekhar, Radiative Transfer, Courier Corporation, 2013.
[52] G.H. Watson Jr., P.A. Fleury, S.L. McCall, Searching for photon localization in the time domain, Phys. Rev. Lett. 58 (9) (1987) 945–948.
[53] K. Yoo, F. Liu, R. Alfano, When does the diffusion approximation fail to describe photon transport in random media? Phys. Rev. Lett. 64 (22) (1990) 2647.
[54] Z.Q. Zhang, I.P. Jones, H.P. Schriemer, J.H. Page, D.A. Weitz, P. Sheng, Wave transport in random media: the ballistic to diffusive transition, Phys. Rev. E Stat. Phys. Plasmas Fluids Relat. Interdiscip. Top. 60 (4 Pt b) (1999) 4843–4850.
[55] R. Elaloufi, W. Carminati, J.J. Greffet, Time-dependent transport through scattering media: from radiative transfer to diffusion, J. Opt. A-Pure Appl. Op 4 (5) (2002) S103–S108.
[56] R.H.J. Kop, P. deVries, R. Sprik, A. Lagendijk, Observation of anomalous transport of strongly multiple scattered light in thin disordered slabs, Phys. Rev. Lett. 79 (22) (1997) 4369–4372.

[57] B. Tallon, T. Brunet, J.H. Page, Impact of strong scattering resonances on ballistic and diffusive wave transport, Phys. Rev. Lett. 119 (16) (2017) 164301.
[58] X. Jia, Codalike multiple scattering of elastic waves in dense granular media, Phys. Rev. Lett. 93 (15) (2004) 154303.
[59] R. Weaver, Ultrasonics in an aluminum foam, Ultrasonics 36 (1–5) (1998) 435–442.
[60] T. Brunet, X. Jia, P. Mills, Mechanisms for acoustic absorption in dry and weakly wet granular media, Phys. Rev. Lett. 101 (13) (2008) 138001.
[61] J. Crank, The Mathematics of Diffusion, Oxford University Press, 1979.
[62] E.A. Habets, Room impulse response generator, Technische Universiteit Eindhoven, Tech. Rep. 2 (2.4) (2006) 1.
[63] B. Singh, G. Ishwarya, M. Gupta, S. Bhattacharyya, Geopolymer concrete: a review of some recent developments, Constr. Build. Mater. 85 (2015) 78–90.
[64] Q. Kong, Innovation in Piezoceramic Based Structural Health Monitoring, University of Houston, 2015. PhD thesis.
[65] S.W. Shin, C.-B. Yun, J.S. Popovics, J.H. Kim, Improved Rayleigh wave velocity measurement for nondestructive early-age concrete monitoring, Res. Nondestruct. Eval. 18 (1) (2007) 45–68.
[66] V. Giurgiutiu, J. Bao, W. Zhao, Active sensor wave propagation health monitoring of beam and plate structures, Smart Structures and Materials 2001: Smart Structures and Integrated Systems, International Society for Optics and Photonics, 2001, pp. 234-245.
[67] J. Morlet, G. Arens, E. Fourgeau, D. Giard, Wave propagation and sampling theory; Part II, sampling theory and complex waves, Geophysics 47 (2) (1982) 222–236.
[68] J. Morlet, G. Arens, E. Fourgeau, D. Giard, Wave propagation and sampling theory—part I: complex signal and scattering in multilayered media, Geophysics 47 (2) (1982) 203–221.
[69] J.-Y. Kim, Velocity of ultrasound diffusion in heterogeneous media and its applications, Ultrasonics 145 (2025) 107476.
[70] M. Ramaniraka, S. Rakotonarivo, C. Payan, V. Garnier, Effect of the Interfacial transition Zone on ultrasonic wave attenuation and velocity in concrete, Cem. Concr. Res. 124 (2019) 105809.
[71] G. Fang, Q. Wang, M. Zhang, Micromechanical analysis of interfacial transition zone in alkali-activated fly ash-slag concrete, Cem. Concr. Compos. 119 (2021) 103990.
[72] W. Li, H. Zhao, K. Wang, Nanocharacterization of Cementitious Composites: Unveiling Properties at Multiscale, Springer Nature, 2025.
[73] A. Lagendijk, B.V. Tiggelen, D.S. Wiersma, Fifty years of Anderson localization, Phys. Today 62 (8) (2009) 24–29.
[74] O.I. Lobkis, R.L. Weaver, Anderson localization of ultrasound in plates: further experimental results, J. Acoust. Soc. Am. 124 (6) (2008) 3528–3533.
[75] J.A. Turner, Scattering and diffusion of seismic waves, Bull. Seismol. Soc. Amer. 88 (1) (1998) 276–283.
[76] J.A. Turner, P. Anugonda, Scattering of elastic waves in heterogeneous media with local isotropy, J. Acoust. Soc. Am. 109 (5 Pt 1) (2001) 1787–1795.
[77] N.P. Trégourès, B.A. van Tiggelen, Generalized diffusion equation for multiple scattered elastic waves, Waves Random Media 12 (1) (2001) 21.
[78] L. Ryzhik, G. Papanicolaou, J.B. Keller, Transport equations for elastic and other waves in random media, Wave Motion 24 (4) (1996) 327–370.
[79] H. Cheng, K. Löer, M.A.N. Hendriks, Y. Yang, Analytical framework for modelling body-wave scattering and diffusion in concrete, Ultrasonics (2026) 108102.
[80] R. Snieder, Coda wave interferometry and the equilibration of energy in elastic media, Phys. Rev. E Stat. Nonlin. Soft Matter Phys. 66 (4 Pt 2) (2002) 046615.
[81] Y. Zhang, T. Planes, E. Larose, A. Obermann, C. Rospars, G. Moreau, Diffuse ultrasound monitoring of stress and damage development on a 15-ton concrete beam, J. Acoust. Soc. Am. 139 (4) (2016) 1691.
[82] Q. Xue, E. Larose, L. Moreau, Locating structural changes in a multiple scattering domain with an irregular shape, J. Acoust. Soc. Am. 146 (1) (2019) 595.
[83] H. Cheng, S. Zhang, Z. Qian, G. Ye, Y. Yang, Evaluating cracking behaviours in precast prestressed alkali-activated concrete (AAC) bridge decks using ultrasonics-based damage indicators, Eng. Struct. 360 (2026) 122675.